# Nickel stanogermanides thin films: Phases formation, kinetics, and Sn segregation

H Khelidj, A Portavoce, K Hoummada, M Bertoglio, M C Benoudia, M Descoins, D Mangelinck

Journal of Applied Physics

RESEARCH ARTICLE | SEPTEMBER 03 2024

# Nickel stanogermanides thin films: Phases formation, kinetics, and Sn segregation

H. Khelidj ; A. Portavoce ; K. Hoummada ; M. Bertoglio ; M. C. Benoudia ; M. Descoins; D. Mangelinck



*J. Appl. Phys.* 136, 095301 (2024)
https://doi.org/10.1063/5.0220979







Journal of Applied Physics ARTICLE pubs.aip.org/aip/jap

# Nickel stanogermanides thin films: Phases formation, kinetics, and Sn segregation

Cite as: J. Appl. Phys. **136**, 095301 (2024); doi: 10.1063/5.0220979
Submitted: 29 May 2024 · Accepted: 12 August 2024 ·
Published Online: 3 September 2024



H. Khelidj,[1,a)] A. Portavoce,[1] K. Hoummada,[1] M. Bertoglio,[1] M. C. Benoudia,[2] M. Descoins,[1] and D. Mangelinck[1]

## AFFILIATIONS

[1]Aix-Marseille University, University of Toulon, CNRS, IM2NP, Marseille, France
[2]École Nationale Supérieure des Mines et de la Métallurgie, L3 M, Annaba, Algeria

[a)]**Author to whom correspondence should be addressed:** hamza.khelidj@im2np.fr

## ABSTRACT

$Ge_{1-x}Sn_x$ thin films with a Sn content of $x \geq 0.1$ present a direct bandgap, which is very interesting for the fabrication of efficient photonic devices. The monostanogermanide phase, Ni(GeSn), is promising to form ohmic contact in GeSn-based Si photonic devices. However, the formation kinetics of Ni stanogermanides and the incorporation of Sn in Ni–GeSn phases are not fully understood. In this work, Ni thin films were deposited on Ge and $Ge_{0.9}Sn_{0.1}$ layers grown in epitaxy on an Si(100) substrate using magnetron sputtering technique. *In situ* x-ray diffraction measurements were performed during the solid-state reaction of Ni/Ge and Ni/$Ge_{0.9}Sn_{0.1}$. 1D finite difference simulations based on the linear parabolic model were performed to determine the kinetics parameters for phase growth. The nucleation and growth kinetics of Ni germanides are modified by the addition of Sn. A delay in the formation of Ni(GeSn) was observed and is probably due to the stress relaxation in the Ni-rich phase. In addition, the thermal stability of the Ni(GeSn) phase is highly affected by Sn segregation. A model was developed to determine the kinetic parameters of Sn segregation in Ni(GeSn).





## I. INTRODUCTION

Silicon photonics has now become a key technology in the actual-generation communication systems and data interconnections.[1–5] The advantage of this technology is the possibility of using the CMOS technology for the integration of photonic components allowing low costs and high production volume.[3] CMOS technology already allows the integration of photonic devices such as Si nitrides-based waveguides, SiGe-based optical modulators, and Ge- and SiGe-based photodetectors.[6–10] Recently, several companies have started manufacturing these photonic components.[11–13] However, efficient CMOS-compatible lasers remain the biggest challenge for silicon photonic light sources.[3,14,15] Indeed, as Si, Ge, and SiGe are indirect bandgap semiconductors, the absorption and emission of a photon are almost inefficient because of the energy loss caused by the phonons. SiGe offers a lattice constant that can be tuned by adjusting the Ge content. However, the lattice mismatch with Si is large for high Ge concentrations, which can introduce defects during the epitaxial growth on Si.[16,17] In recent years, $Ge_{1-x}Sn_x$ alloys have attracted attention for the realization of devices compatible with Si technology, operating in the medium infrared (MIR) and near infrared (NIR) spectrum region.[18–22] These alloys have the advantage of being group IV semiconductors, and they are compatible with CMOS processes. The addition of tin, which is a zero bandgap semi-metal in the α-Sn phase (gray tin) with a diamond structure, can transform Ge into a direct gap semiconductor. The $Ge_{1-x}Sn_x$ alloy is expected to exhibit a direct bandgap for Sn concentration larger than about 10 at. % ($x = 0.1$), which is very promising for the fabrication of an efficient laser.[23–29]

However, there is a large difference in lattice parameter between the Sn and the Ge diamond structures. As the lattice parameter of Sn (0.649 nm) is about 14% greater than that of Ge (0.565 nm),[30–32] the lattice parameter of the alloy increases with increasing Sn content.[33–35] To produce a single-crystal $Ge_{1-x}Sn_x$ alloy, substrates with a lattice parameter close to the one of $Ge_{1-x}Sn_x$ are required. However, the growth of semiconductors is carried out on an Si substrate in CMOS technology. Because of the large lattice mismatch between the Si substrate ($a_{Si} = 0.543$ nm)[36,37] and the $Ge_{1-x}Sn_x$ alloy ($a_{GeSn} > 0.565$ nm), the epitaxial growth of

$Ge_{1-x}Sn_x$ is very difficult to achieve without generating dislocations at the interface or in the film. In recent years, several techniques for growing thin-film semiconductors have enabled to fabricate epitaxial layers of $Ge_{1-x}Sn_x$ of good quality. Molecular beam epitaxy (MBE) and chemical vapor deposition (CVD) are the best-known techniques for the epitaxial growth of semiconductors. Although high-quality $Ge_{1-x}Sn_x$ alloys have been grown by these techniques, further research has been conducted on the use of more economical methods, such as magnetron sputtering. This deposition technique is widely used for the fabrication of ohmic contacts in CMOS technology.[38,39] It can also be used to deposit insulators, amorphous and crystalline semiconductor films.[40] Magnetron sputtering offers great potential for mass production of $Ge_{1-x}Sn_x$ alloys. Recent works demonstrated that single crystals of $Ge_{1-x}Sn_x$ can also be produced on Si(100) at low temperatures using Ge buffer deposited by magnetron sputtering.[41–45] The produced $Ge_{1-x}Sn_x$ layers have similar quality compared to the ones obtained by MBE and CVD.[41–45]

From the devices' point of view, recent experiments have shown that $Ge_{1-x}Sn_x$ alloys have higher hole mobility than Ge.[46] Han *et al.* successfully fabricated a $Ge_{1-x}Sn_x$ channel p-MOSFET using a CMOS-compatible process at 370 °C.[47] Its structure is composed of a source and a drain using nickel stanogermanide as contact.[47] These $Ge_{1-x}Sn_x$ p-MOSFETs exhibit a hole mobility of 430 $cm^2/V$ s that is 66% higher than that of Ge p-MOSFETs, with a 64% reduction in contact resistance.[47] Indeed, semiconductor-based electronic and optoelectronic devices need not only high charge mobility but also low effective ohmic contact to receive and deliver signals. Tungsten W is not typically used for contacts in microelectronics due to its tendency not to form compounds with high resistivity. Moreover, its work function is not optimal for some semiconductor materials, and it usually forms high Schottky barriers.[48] The addition of Pt in NiPt alloys significantly enhances the thermal and chemical stability of the stanogermanide, reducing diffusion issues and improving the overall reliability of the contacts.[49] However, a higher resistivity comparing to Ni stanogermanide and the added complexity for theoretical study can pose challenges.[50] For $Ge_{1-x}Sn_x$-based devices, Ni stanogermanides have been proposed as ohmic contacts to achieve low contact resistance (Rc) and low sheet resistance ($R_{sh}$).[51–57] However, understanding the formation kinetics of Ni stanogermanides and the incorporation of Sn into Ni–GeSn phases is important for devices' fabrication and reliability and requires extensive studies. Depending on the alloy composition, Sn could (i) be soluble in the Ni–Ge phases, (ii) segregate at grain boundaries, and/or (iii) form Ni–Sn alloys.[54,58] Each of these behaviors will have different impacts on the growth and properties of the phases such as the thermal budget needed to obtain the desired phase (i.e., Ni mono-stanogermanide), crystallographic texture, agglomeration, as well as the electrical properties of the contact. This paper presents the study of the Ni stanogermanides' formation. 20 nm of Ni film was deposited on $Ge_{1-x}Sn_x$ epitaxially grown on Si(100) by magnetron sputtering. The formation sequence of the phases with and without Sn as well as the growth kinetics are studied. The effect of stress relaxation on the formation of Ni(GeSn) is shown. The kinetics of Sn segregation out of the Ni(GeSn) phase is also determined, using *in situ* x-ray diffraction (XRD) and finite differences simulation.

## II. EXPERIMENTS

Two types of samples constituted of Ni/Ge/Si(100) and Ni/$Ge_{0.9}Sn_{0.1}$/Ge/Si(100) stacks were prepared for this work [Figs. 1(a) and 1(b)]: in the following, they will be called Ni–Ge and Ni–GeSn samples even if their structures are more complex than their given name. The Si(100) substrates were dipped in a 5% HF solution in

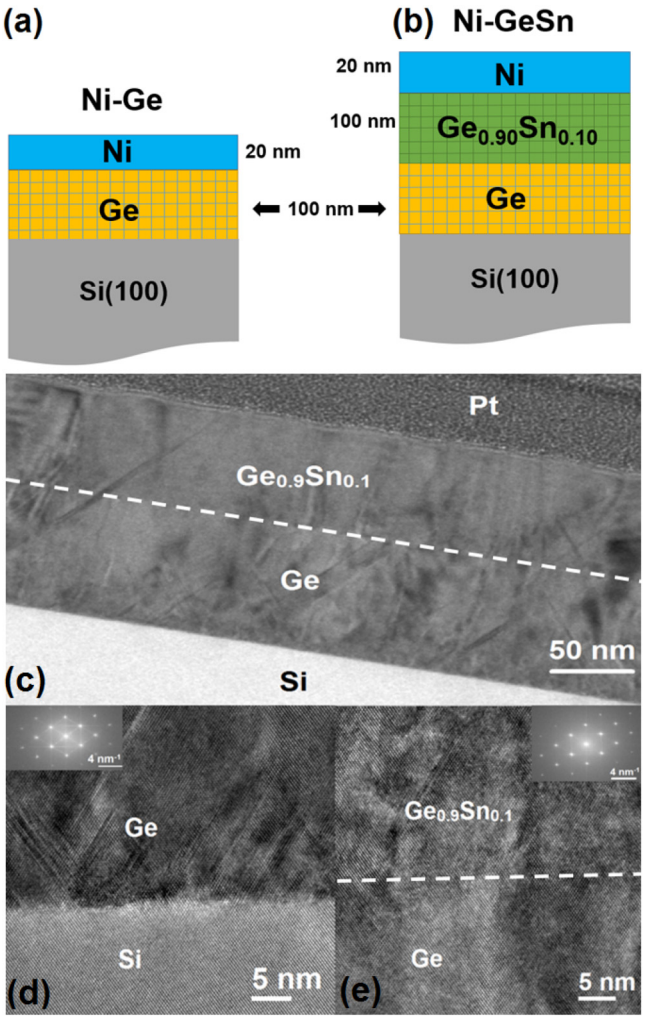


**FIG. 1.** (a) and (b) Schematics of the Ni–Ge and Ni–GeSn sample configurations prepared by magnetron sputtering: 100 nm of Ge was deposited on Si(100) at 360 °C for both samples. During the cooling process, 100 nm of $Ge_{0.9}Sn_{0.1}$ was deposited on the Ge buffer. Finally, a 20 nm Ni layer was deposited at room temperature on both the Ge and $Ge_{0.9}Sn_{0.1}$ layers. Cross section transmission electron microscopy (TEM) images of $Ge_{0.9}Sn_{0.1}$/Ge/Si(100) films (Ni–GeSn sample): (c) Complete view of the films by scanning transmission electron microscopy (STEM), the platinum (Pt) layer was used as a protective film. (d) High-resolution TEM image at the Ge/Si interface. (e) High-resolution TEM image at the $Ge_{0.9}Sn_{0.1}$/Ge interface. The insets in (d) and (e) present the Fast Fourier Transform (FFT) obtained from the images, showing the epitaxial registry between the Si substrate, Ge buffer, and $Ge_{0.9}Sn_{0.1}$.

order to remove the Si native oxide before to be loaded in the sputtering system. Following this cleaning, either only a 100 nm Ge buffer layer or a 100 nm $Ge_{0.9}Sn_{0.1}$ layer on the Ge buffer layer was deposited on the Si(100) substrate in DC mode using a 99.9999% pure Ar gas flow in the magnetron sputtering system exhibiting a base pressure of $10^{-8}$ Torr. In this setup, the samples are mounted on a horizontal rotating sample holder. The system allows for three targets to be placed symmetrically at 120° angles from each other, positioned 45° between the normals of the target surfaces and the sample surface. Deposition was carried out at a pressure of $2.25 \times 10^{-3}$ Torr. The samples were fixed to a steel plate using metal screws and rotated at a speed of 5 rpm. The sample holder was heated through radiative effects using an electrical resistance heater placed underneath. Temperature measurements were taken using type K thermocouples (THERMOCOAX). The Ge buffer layer was deposited on Si(100) at $T = 360$ °C from a 99.999% pure Ge target. For the Ni–GeSn sample, the $Ge_{0.9}Sn_{0.1}$ layer was co-deposited from the Ge target and a 99.99% pure Sn target after stopping the sample heater, with no growth interruption between the Ge buffer and $Ge_{0.9}Sn_{0.1}$. As the cooling rate is low in the sputtering system, the $Ge_{0.9}Sn_{0.1}$ deposition temperature ranges between 350 and 360 °C, which is similar to the deposition temperature for Ge buffer. On both samples, 20 nm of Ni was deposited at room temperature by DC magnetron sputtering using a 99.999% pure Ni target without breaking the vacuum after the deposition of $Ge_{1-x}Sn_x$ (x = 0 and x = 0.1) layers.

Structural observations were performed using transmission electron microscopy (TEM). Scanning TEM dark-field (STEM-DF) imaging at 200 keV was conducted using a LaB6 Thermo Fisher Tecnai TEM equipped with an OXFORD X-max80 silicon drift detector. The results are presented in Fig. 1(c). High-resolution TEM images were acquired [Figs. 1(d) and 1(e)] at 200 keV using a Thermo Fisher Titan microscope with a field emission gun and a spherical aberration (Cs) correction system. A Cs value between 0 and −0.05 mm was used, allowing a point-to-point resolution of approximately 1 Å to be achieved. The TEM measurements confirmed that the Ge and $Ge_{0.9}Sn_{0.1}$ films are fully monocrystalline with a diamond structure, exhibiting no amorphous regions. Figure 1(d) clearly shows misfit dislocations at the Si/Ge interface, as well as threading dislocations caused by the significant lattice mismatch between Ge and Si. The density of these misfit dislocations is reduced at the Ge/$Ge_{0.9}Sn_{0.1}$ interface, as seen in Fig. 1(e). The fast Fourier transform (FFT) from high-resolution TEM images illustrates the epitaxial configuration among the Si substrate, Ge buffer, and $Ge_{0.9}Sn_{0.1}$ layers. These results demonstrate that the epitaxial growth of $Ge_{1-x}Sn_x$ on Si (001) is achievable due to the application of a Ge buffer layer deposited via magnetron sputtering.

X-ray reflectivity was carried out at room temperature (RT) to determine the thicknesses of sputtered films deposited in different conditions. The structure of the films was studied by x-ray diffraction (XRD) in the $\theta$–$\theta$ geometry using a Cu $K_\alpha$ source ($\lambda_{K\alpha} = 0.154$ nm) in a PANalytical X'Pert PRO setup equipped with an X'Celerator detector designed for high-speed data collection. This setup was used to perform *in situ* XRD measurements during solid state reaction between $Ge_{1-x}Sn_x$ and Ni. Two types of *in situ* XRD measurements were performed: isothermal annealing and annealing with increasing temperatures by constant steps (denoted by step annealing in the following). For step annealing, the temperature was raised from 50 to 550 °C by steps of 5 °C with a heating ramp of 5 °C min$^{-1}$ and separated by 5 min-long XRD measurements at each temperature step: this step annealing corresponds to an average heating ramp of 1 °C min$^{-1}$. Isothermal *in situ* XRD measurements were also carried out at different temperatures by using a ramp of 10 °C min$^{-1}$ from room temperature to the set temperature and then by continuously performing the 5 min-long XRD measurements. The composition of the layers was determined using Rutherford backscattering spectrometry (RBS) and atom probe tomography (APT). For RBS, 2.0 MeV alpha particles were employed, with a backscatter detector positioned at 170°. Scanning electron microscopy (SEM) imaging as well as transmission electron microscopy (TEM) and APT sample preparations were carried out using an FEI dual-beam HELIOS 600 nanolab. APT measurements were conducted at 50 K with a laser-pulsed CAMECA LEAP 3000X HR microscope, operating at a laser pulse frequency of 100 kHz and a laser power of 0.2 nJ. The surface topography of the layers was studied using atomic force microscopy (AFM). AFM images were obtained in a non-contact mode using a PSIA XE-100 in an air microscope. Film sheet resistance was measured using the four-point probe method.

## III. RESULTS

The solid-state reaction for the Ni–Ge sample was followed by *in situ* XRD step annealing as shown in Fig. 2(a) as a contour map. This contour map represents a succession of XRD diffractograms that allows a three-dimensional presentation in planar view of the XRD measurements: the x-axis corresponds to the diffraction angle $2\theta$, the y-axis to the temperature ranging from 50 to 550 °C, and the diffracted intensity is characterized by the shades of colors going from blue to red, representing, respectively, the lowest to the highest intensities. All the obtained diffractograms were measured in the $2\theta$ range between 20° and 67°. An additional XRD measurement was performed at room temperature (RT) in the same conditions just before the *in situ* XRD measurement. From RT to about 140 °C, the Ni (111) and (200) XRD peaks corresponding to the face centered cubic (FCC) structure are observed at 44.6° and 52.1°, respectively. The Ge (400) XRD peak at 65.98° corresponding to the diamond structure is the only peak detected for the Ge film; it corresponds to the same orientation than the substrate Si (400) diffraction peak as expected for an epitaxy. From $T = 150$ °C, a peak at 31.5° characteristic of the Ni-rich phase [$Ni_5Ge_3$ (101)] with a hexagonal structure is observed.[46] At $T = 200$ °C, considering the detection limit of the XRD, the Ni XRD peaks have totally disappeared, indicating to the full consumption of the Ni layer to form a $Ni_5Ge_3$ phase. From this temperature (200 °C), the $Ni_5Ge_3$ (101) XRD peak starts to shift toward high angles. At $T \sim 205$ °C, five diffraction peaks corresponding to the NiGe phase are observed simultaneously, with the NiGe (111) and NiGe (301) peaks being the most intense. The intensity of the NiGe phase peaks increases with increasing temperatures, at the same time as $Ni_5Ge_3$ is consumed. At $T = 500$ °C, the diffraction peaks of the NiGe phase start to disappear with the appearance of new peaks that probably correspond to the $NiSi_{1-x}Ge_x$ phase.[59]

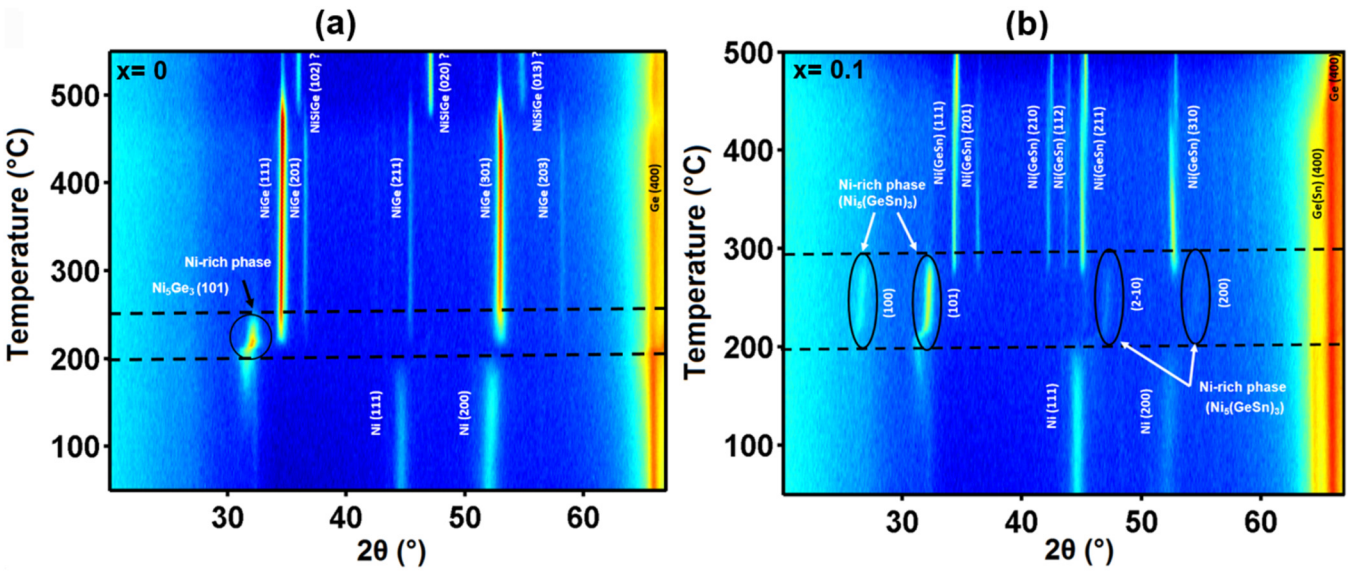


**FIG. 2.** *In situ* XRD measurements performed during step annealing following an average ramp of ~1 °C min$^{-1}$ from 50 to $T$ = 550 °C: (a) Ni–Ge sample; (b) Ni–GeSn sample.

Figure 2(b) presents the *in situ* XRD measurement during step annealing from 50 to 500 °C for the Ni–GeSn sample [20 nm Ni/100 nm $Ge_{0.9}Sn_{0.1}$/100 nm Ge buffer/Si (100) substrate]. At room temperature, only the (400) diffraction peak is observed for the phases with the diamond structure ($Ge_{0.9}Sn_{0.1}$, Ge, and Si), indicating that the Ge and $Ge_{0.9}Sn_{0.1}$ layers display an epitaxial relationship with the Si substrate. A similar solid-state reaction sequence is obtained for the Ni–GeSn system than for the Ni–Ge system with the formation of $Ni_5(GeSn)_3$ followed by the one of Ni(GeSn). However, differences were observed concerning the thermal stability and the texture of the Ni-rich phase and Ni-monostanogermanide. The first important change concerns the formation of the Ni(GeSn) phase that is delayed compared to the NiGe phase. More precisely, there is a gap in temperature between the end of the Ni consumption (and, thus, the full formation of the Ni-rich phase) and the beginning of Ni(GeSn) formation. In contrast, NiGe starts to form just after the disappearance of the Ni XRD peak. This also means that the Ni-rich phase is present on a larger temperature range for the Ni–GeSn sample than for the Ni–Ge sample. Another interesting point is that the positions of the XRD peaks of NiGeSn are shifting to larger values when temperature is increased. This is certainly due to the rejection of Sn from Ni(GeSn). These points will now be studied in more detail by performing *in situ* XRD during isothermal annealing. In order to study the formation and growth kinetics of the $Ni_5(GeSn)_3$ phase, three *in situ* isothermal annealing was carried out at different temperatures (150, 170, and 180 °C) for the Ni–GeSn sample. The annealing temperatures were selected to have only the formation of the Ni-rich phase.

Figure 3 presents the *in situ* XRD maps of isothermal experiment at 170 °C that is representative of these three *in situ* annealing. It shows that the growth of the $Ni_5(GeSn)_3$ phase is linked to the consumption of the Ni film. After the total consumption of the Ni layer, the diffraction peaks of the Ni-rich phase shift toward high angles, and their intensity increases as in the case of step annealing (Fig. 2). The (400) XRD peaks corresponding to the diamond structures ($Ge_{1-x}Sn_x$, Ge, and Si) are detected during three isothermal annealing.

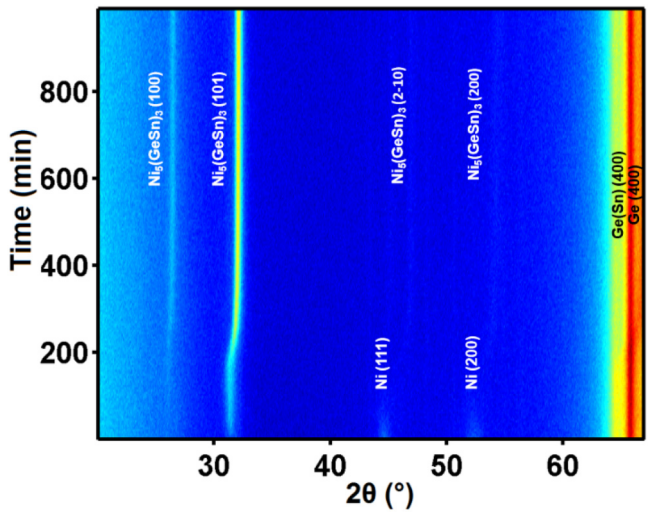


**FIG. 3.** *In situ* XRD measurement performed during the isothermal annealing of the Ni–GeSn sample at $T$ = 170 °C.

Figures 4(a)–4(c) show the normalized intensities of the Ni (111) and the $Ni_5(GeSn)_3$ (101) peaks as a function of time, for the isothermal *in situ* XRD measurements at 150, 170, and 180 °C of the Ni–GeSn sample. By increasing the annealing temperature, the Ni layer is consumed faster: for example, during annealing at 150 °C, the Ni has totally disappeared after ~650 min, while at 180 °C, the Ni is fully consumed after ~93 min. Furthermore, the intensity of the Ni-rich phase increases with time for each temperature even when the Ni layer is fully consumed, until it stabilizes and forms a plateau. The time to reach the plateau (before intensity stabilization) decreases with increasing annealing temperature. To study the formation and growth kinetics of the Ni(GeSn) phase, *in situ* XRD measurements during isothermal annealing at 260 and 270 °C were also carried out. The *in situ* XRD map at 260 °C is presented in Fig. 4(a) and shows the consumption of the $Ni_5(GeSn)_3$ phase from the beginning of the experiment.

The consumption of the Ni-rich phase is accompanied by the appearance of the Ni(GeSn) with the same diffraction peaks than the ones observed for step annealing [Fig. 2(b)]. This phase persists until the end of the annealing. The $Ge_{1-x}Sn_x$ (400) and Ge (400) peaks are detected during all isothermal annealing. Figures 4(b) and 4(c) show the normalized integrated intensity of the $Ni_5(GeSn)_3$ (101) peak as well as the Ni(GeSn) (111) peak as a function of time for isothermal annealing at 260 and 270 °C, respectively. For each temperature, the intensity of the $Ni_5(GeSn)_3$ phase decreases with time, while that of the Ni(GeSn) phase increases until forming a plateau, indicating that the growth of the phase is finished. The time before stabilization of the intensity for annealing at 270 °C is shorter (~100 min) than that for annealing at 260 °C (~150 min). Isothermal *in situ* XRD measurements were also carried out at high temperature (≥350 °C) in order to examine the kinetics of Sn segregation in the Ni–GeSn sample.

## IV. DISCUSSION

### A. Phase sequence: Comparison between the two systems

The goal of this paper is to study the thin film reaction between Ni and Ge(Sn) to create contacts for microelectronics and photonics. For these applications, the thickness of the contact must be limited to a few tens of nanometers, and the contact is formed by the reaction of a metal thin film with a semiconductor substrate to form an intermetallic compound with low resistivity. In this configuration, the thickness of the contact is controlled by the metal thickness since the metal quantity is limited (for example, the NiGe thickness is approximately twice the Ni thickness). Therefore, the choice of 20 nm of Ni was dictated by the applications in photonics. As explained hereafter, this thickness corresponds to the thin film regime of metal–semiconductor reaction.

This study is, thus, focused on the solid-state reaction between a 20 nm Ni thin film with a 100 nm layer of $Ge_{0.9}$–$Sn_{0.1}$, and a comparison is made with the pure Ge layer. For both systems, the sequential formation of two phases is observed: the Ni-rich phase with the hexagonal structure, $Ni_5Ge_3$ and $Ni_5(GeSn)_3$, and the orthorhombic phase, NiGe and Ni(GeSn). For the Ni–$Ge_{0.9}Sn_{0.1}$ system, Quintero *et al.* have also observed a sequential growth of these two phases $Ni_5(GeSn)_3$ and Ni(GeSn).[52] However, in the case of the Ni–Ge system, previous works have reported either the simultaneous growth[60] or the sequential growth[61] of the two phases ($Ni_5Ge_3$ and NiGe). The comparison of *in situ* XRD maps (Fig. 2) shows that the solid-state reaction sequences are similar for both kinds of samples (0% and 10% Sn).

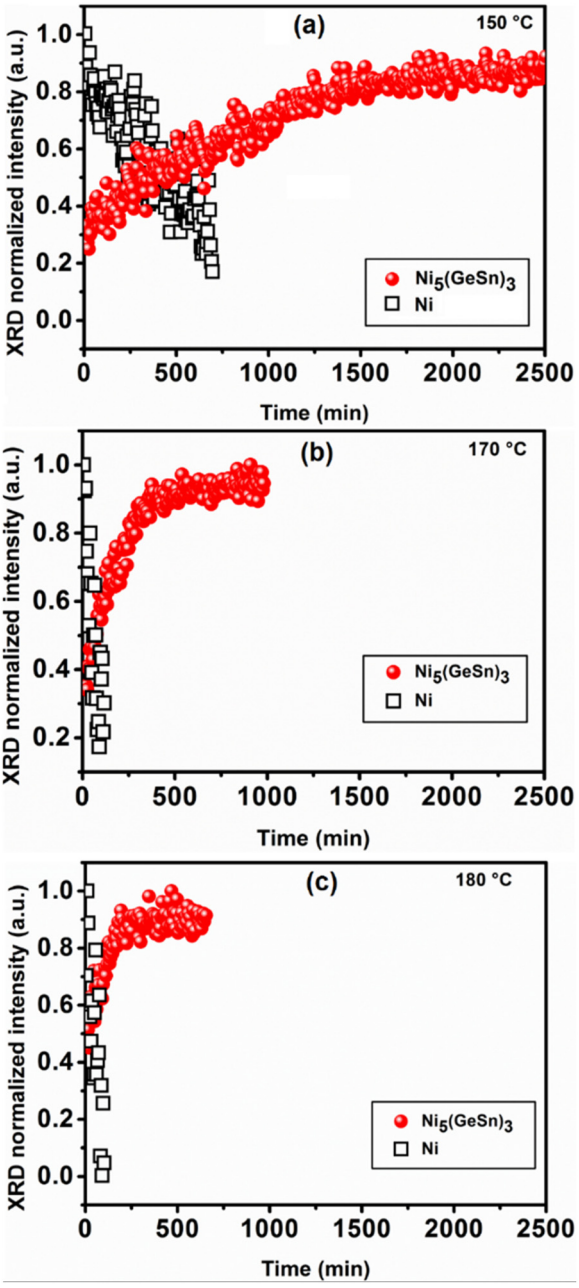


**FIG. 4.** Integrated and normalized intensity of the Ni and $Ni_5(GeSn)_3$ XRD peaks vs temperature during three *in situ* isothermal annealing of the Ni–GeSn sample at (a) 150, (b) 170, and (c) 180 °C.

The sequential formation of some stable or metastable phases is one of the specific characteristics of the thin film reaction.[62,63] We will first provide insights for the binary metal–semiconductor (SC) system, specifically the Ni–Ge system, then discuss the Ni–Ge–Sn ternary system, and finally propose explanations for the absence of Ni–Sn intermetallic formation.

In bulk binary diffusion couples, all the phases present in the phase diagram at the temperature of interest typically form simultaneously. For these bulk diffusion couples, the square of the thickness of each phase is proportional to the time and depends mainly on the diffusion coefficient in the growing phases. However, thin film reactions are usually characterized by the sequential formation of certain phases, which may be stable or metastable. This behavior, i.e., sequential formation of selected phases, is often explained by kinetics competition and/or nucleation limitations.[62,63] In this sense, the products of the thin film reaction may be considered metastable. However, the final product of the metal/SC thin film reaction is usually the intermetallic containing the highest content of the SC in contact with the SC substrate (for example, NiGe/Ge in the Ni–Ge system). This corresponds to equilibrium since the solubility of metal in an SC is usually very low. Therefore, even if the amount of metal is very limited compared to the amount of SC due to the respective thickness of the metal film and SC substrate (i.e., $x_{SC}$ is almost equal to 1), the system is in the two-phase domain. For the Ni–Ge system, this corresponds to a thin film of NiGe on the Ge substrate. Consequently, the final result does not depend on Ge or Ge(Sn) thickness as long as it is larger than the thickness needed to form NiGe (about 2.4 times the Ni thickness). The thin film regime, i.e., sequential formation of selected phases, is usually observed when the Ni thickness is between about 10 and 100–200 nm. For Ni thicknesses smaller than 10 nm, usually called the very thin film regime, other phases can be stabilized by strong interfacial energy effects. For thicknesses larger than 100–200 nm, the simultaneous growth of several stable phases occurs similarly to bulk diffusion couples. To summarize, for Ni thicknesses between about 10 and 100–200 nm, sequential formation is usually observed, and the final result corresponds to the SC-rich intermetallic in equilibrium with the SC substrate (NiGe–Ge equilibrium). This final result depends neither on the Ni thickness nor on the Ge thickness (for sufficiently large values of this thickness) except that the thickness of this intermetallic (NiGe) is larger for larger Ni thicknesses. This is mainly due to the stoichiometry of NiGe and the very low solubility of Ni in Ge.

The situation is different for the Ni–Ge(Sn) reaction because Ge(Sn) is already out of equilibrium (metastable epitaxy) after deposition, as the solubility of Sn in Ge is below 1%, much lower than the 10% incorporated in the Ge(Sn) film. Under heat treatment, the Ge(Sn) film will decompose into Sn and Ge with a small content of Sn, as observed in several studies, including our previous work.[41] Although the ternary phase diagram is not known for Ni concentrations below 55%, the final equilibrium should be a three-phase domain with NiGe, Ge(Sn), and Sn, in accordance with our observed final result: the simultaneous presence of NiGe, Ge(Sn), and Sn. Accordingly, a schematic Ni–Ge–Sn ternary phase diagram is shown in Fig. 5. In Fig. 5, the system concentration, considering the thicknesses of the Ni and Ge(Sn) layers, is indicated by a blue cross for the Ni–Ge (10% Sn) ternary system and is located inside the three-phase domain (NiGe–Ge–Sn). In this case, the final result should also not depend on the Ni thickness or the Ge(Sn) thickness as long as the system concentration falls in this three-phase domain. This is primarily due to the fact that NiGe, Ge, and Sn solid phases are almost stoichiometric. A change in the relative thicknesses of Ni and Ge (10% Sn) layers will only alter the proportion of the three phases.

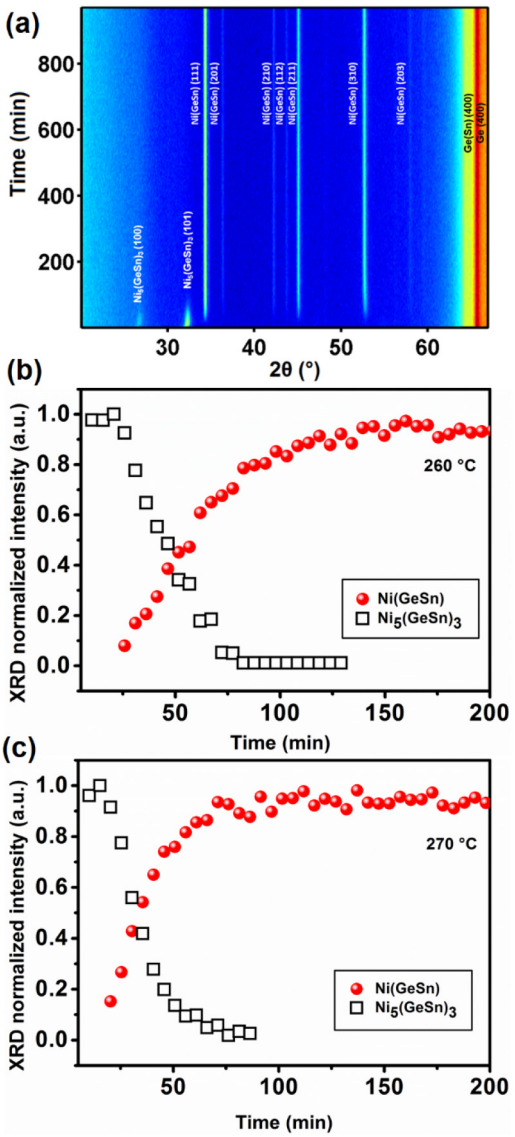


**FIG. 5.** *In situ* XRD measurements performed during the annealing: (a) contour map at $T$ = 260 °C, (b) and (c) integrated and normalized intensity of the $Ni_5(GeSn)_3$ (101) and Ni(GeSn) (111) XRD peaks vs temperature during *in situ* isothermal annealing at 260 and 270 °C, respectively.

No Ni–Sn intermetallics have been observed in our results, in accordance with most studies on the Ni–Ge–Sn thin film reaction.

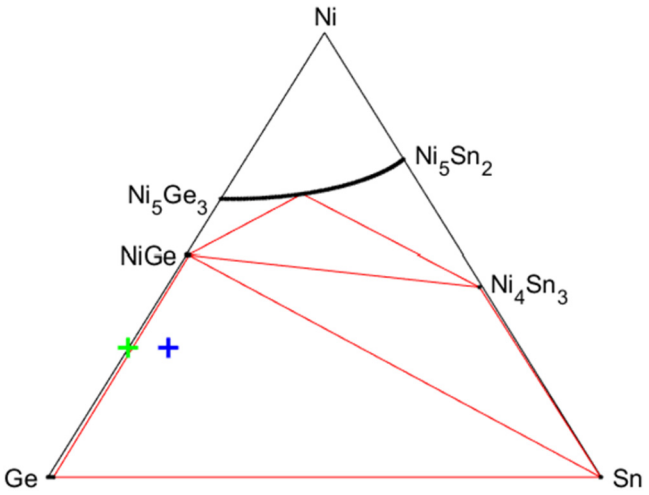


**FIG. 6.** Schematic isothermal section of the Ni-Ge-Sn ternary phase diagram for temperatures below the melting temperature of Sn (231.9°C). Only the phases relevant to the thin film reaction are shown. The red lines correspond to three-phase domains. The global concentration of the system, constituted by the Ni and Ge (or GeSn) layers, is indicated by a green cross for the Ni-Ge binary system and by a blue cross for the Ni-Ge(10%Sn) ternary system. These crosses correspond to a NiGe-Ge equilibrium and a NiGe-Ge-Sn equilibrium, respectively.

Only one study[58] reported the NiSn phase, but this phase was identified with two very low-intensity XRD peaks, and NiSn is a metastable phase.

The absence of Ni–Sn intermetallics might be due to the relatively low concentration of Sn in the Ge film (10%) and the high solubility of Sn in some germanides. Indeed, in the bulk Ni–Ge–Sn phase diagram,[64] $Ni_5Ge_3$ and $Ni_5Sn_2$ form a continuous solid solution. Thus, during the first phase growth, the 10% of Sn will be incorporated into $Ni_5Ge_3$ without forming Ni–Sn intermetallics.

After the formation the first stanogermanide, $Ni_5(Ge,Sn)_3$, Ni–Sn intermetallics may also appear during or after the formation of NiGe. The solubility of Sn in NiGe is not known but might be relatively low because we observed that Sn is rejected from NiGe at temperatures above 550 °C. In this case, the absence of Ni–Sn intermetallics is, thus, not related to solubility but might be related to the growth of the stanogermanides with metastable composition. Indeed, Ni is expected to be the fast diffusing species in the Ni stanogermanides, as is the case for Ni germanides and Ni silicides. The growth of the stanogermanides will, thus, occur by the diffusion of Ni in these phases, while Ge and Sn do not practically diffuse and are, thus, incorporated into the growing phase. This behavior allows the incorporation of more Sn than the equilibrium solubility of Sn in the germanide and could, thus, delay or suppress the growth of Ni–Sn intermetallics.

Finally, the observed final result of the Ni–Ge (10% Sn) thin film reaction (i.e., after sufficient time and temperature annealing) consists of three phases: NiGe, Ge(Sn), and Sn. As already discussed, this should correspond to a three-phase equilibrium state for the global concentration of the system, including the Ni layer

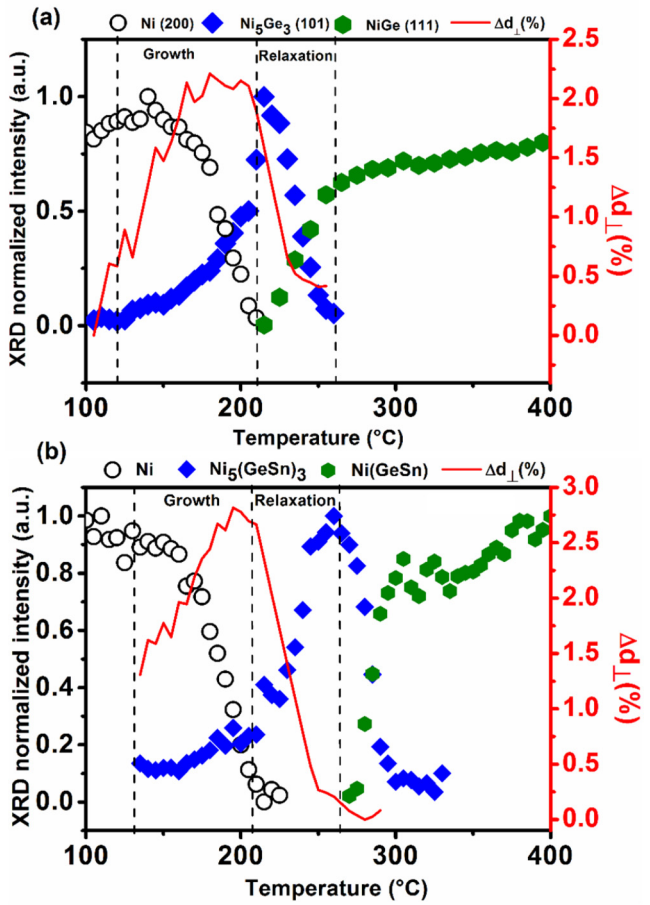


**FIG. 7.** Evolution of the normalized intensity of XRD peaks (left axis) and relative variation of the interpalanar spacing $\Delta d_\perp$ (right axis) during *in situ* step annealing for: (a) Ni-Ge system, (b) $Ni\text{-}Ge_{0.9}Sn_{0.10}$ system.

and the Ge(Sn) layer, as illustrated in Fig. 5. Therefore, no Ni–Sn phases are expected as a final result in the Ni–Ge (10% Sn) ternary system.

Even if the phase sequence is similar for the thin film reaction without Sn or with 10% Sn, differences in the stability temperature range of the two phases are observed between the Ni–Ge and Ni–GeSn samples. In addition, the texture of Ni monostanogermanide is also different. This part of the study will be detailed later. These differences suggest that the phase sequence is not affected by the presence of Sn, but that the nucleation and growth kinetics of Ni germanides are modified by the addition of Sn.

### B. $Ni_5(GeSn)_3$ phase formation

Figure 6 shows the evolution of the normalized XRD intensity of the different phases for the Ni–Ge and $Ni\text{–}Ge_{0.9}Sn_{0.1}$ systems during step annealing (Fig. 2). In the case of Ni–Ge system

[Fig. 6(a)], the end of the growth of $Ni_5Ge_3$ phase coincides with the total consumption of Ni and the start of the NiGe phase formation. However, for the Ni–$Ge_{0.9}Sn_{0.1}$ system, the intensity for $Ni_5(GeSn)_3$ still increases after the total consumption of Ni. This behavior is non-trivial since the growth of $Ni_5(GeSn)_3$ occurs by consumption of the Ni film. As already mentioned, Fig. 2(b) and 7(a) show that the XRD peaks shift during annealing indicating some changes in the lattice parameters of the $Ni_5(GeSn)_3$ phase. Specifically, there is a shift toward high angle after the full consumption of the Ni film associated to a lattice reduction. This phenomenon may be related to a change in composition or a relaxation of mechanical stresses. More specifically, XRD measurements in $\theta$–$\theta$ geometry are sensitive to the distance between the crystallographic planes that are parallel to the surface and, therefore, the distance $d_\perp$ perpendicular to the surface. The relative variation in the distance $\Delta d_\perp$ between the parallel crystallographic planes in the $Ni_5Ge_3$ and $Ni_5(GeSn)_3$ phases can be determined by the following relationship:[65]

$$\Delta d_\perp = \frac{d_\perp - d_{\min}}{d_{\min}}, \tag{1}$$

where $d_{\min}$ is the minimum distance of $d_\perp$. This variation $\Delta d_\perp$ is represented in red (right axis) in Fig. 6. A fast reduction in $\Delta d_\perp$ when the Ni layer is completely consumed is observed, which is associated with the increase in the intensity of the $Ni_5(GeSn)_3$ XRD peak. Knowing that there is no more Ni available for the growth of the Ni-rich phase, this increase in intensity must be related to a phenomenon other than the phase growth. Furthermore, the beginning of the formation of the Ni(GeSn) phase takes place when $\Delta d_\perp$

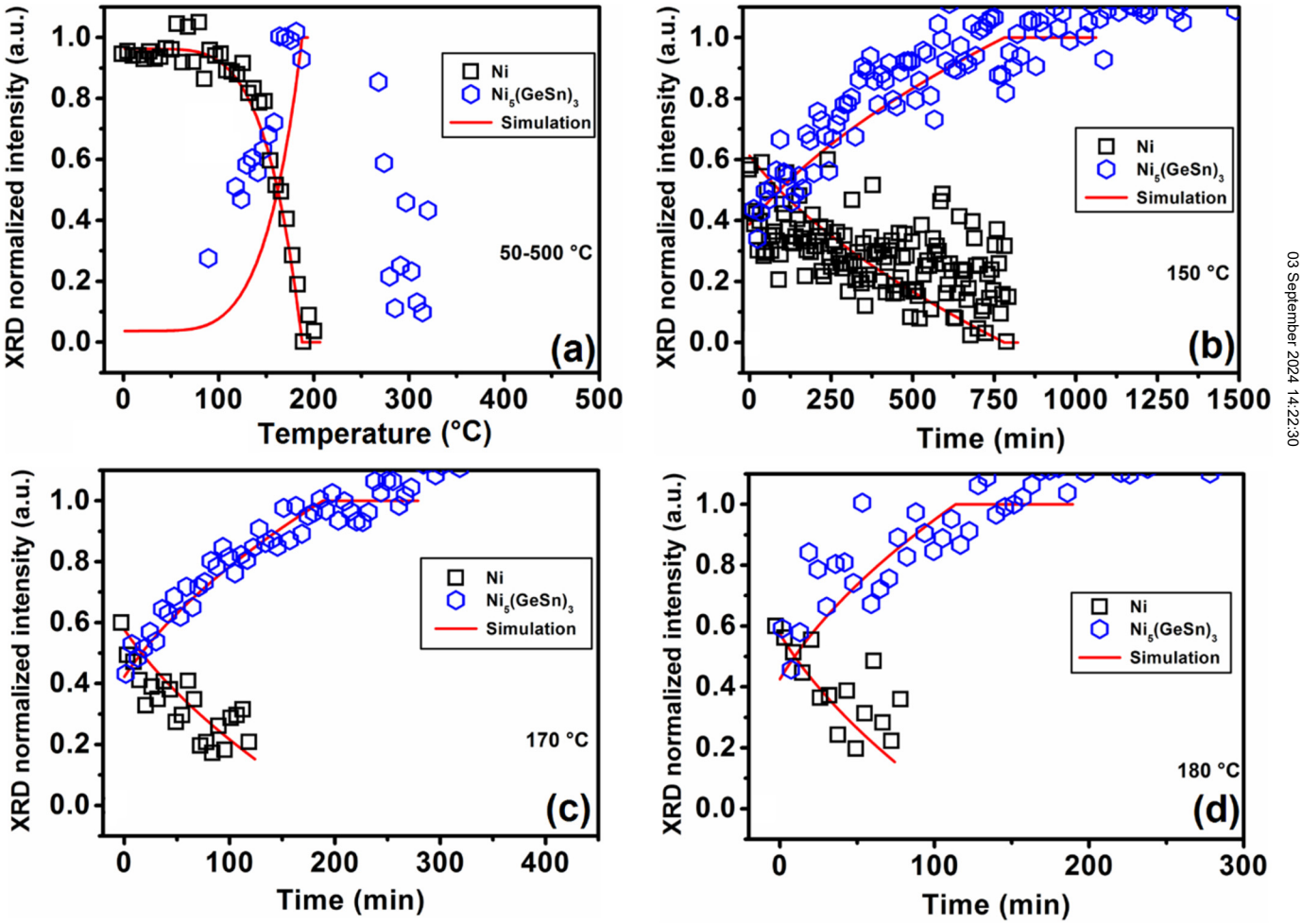


FIG. 8. Simulation of growth controlled by the diffusion in the $Ni_5(GeSn)_3$ phase using *in situ* XRD experiments carried out for Ni–GeSn sample: (a) by step, (b) isothermal at $T = 150$ °C, (c) isothermal at $T = 170$ °C, and (d) isothermal at $T = 180$ °C. The kinetic parameters are the same for all the experiments. Since the XRD intensity are relatively noisy, three isothermal XRD annealing were performed in addition to the step annealing in order to better determine the kinetic parameters.

reaches a minimum. During the formation of $Ni_5Ge_3$ and $Ni_5(GeSn)_3$ phases, two stages are, therefore, observed (Fig. 6): the first corresponds to the growth of the phase until the end of Ni consumption, while the second corresponds to a significant decrease in the lattice parameters of the phase (relaxation). In the case of $Ni_5Ge_3$, the relaxation seems to have occurred before the end of the growth without a significant impact on the formation of the phases [Fig. 6(a)]. Nevertheless, the formation of the Ni(GeSn) phase begins after the relaxation is finished [Fig. 6(b)]. The discussion on the $Ni_5(GeSn)_3$ phase will, thus, be separated into two sections. The first one will be devoted to the study of the growth kinetics (when Ni is still present). In the second section (after the total consumption of the Ni layer), the change of the lattice parameters in the $Ni_5(GeSn)_3$ phase will be treated.

### C. $Ni_5(GeSn)_3$ growth kinetics

*In situ* XRD measurement can be used to determine the crystalline structure of phases and also their quantity. Indeed, assuming that the evolution of the microstructure is negligible, the diffracted intensity of the peaks is proportional to the volume of the phase. Since the surface of the sample is constant, the thickness is the only variable, which changes during the phase formation. The increase in the volume of the phase can then be related to the variation in its thickness $L$. Under these assumptions, the evolution of the thickness is proportional to the evolution of the diffracted intensity. The growth kinetics of reactive diffusion in thin films is usually fitted by the Deal and Groves law [Eq. (2)] that takes into account both the diffusion and the interfacial contribution,[66–68]

$$\frac{dL(t)}{dt} = \frac{D}{L + D/K}\frac{\Delta\mu}{k_B T}, \tag{2}$$

with $K$ being the interface kinetic parameter, $D$ being the effective diffusion coefficient, and $\Delta\mu$ being the chemical potential difference through the growing phase.

The interfacial reaction $K$ as well as the diffusion rate $D$ follow an Arrhenius law according to the following equations:[67]

$$K = K_0 \exp\left(-\frac{E_k}{kT}\right), \tag{3}$$

$$D = D_0 \exp\left(-\frac{E_d}{kT}\right), \tag{4}$$

with $K_0$ and $D_0$ being the exponential pre-factors, and $E_k$ and $E_d$ being the activation energy of the reaction and diffusion, respectively.

Figure 8 shows the simulations of the "growth" part (i.e., when there is still an XRD peak for Ni), which are carried out only by taking into consideration the formation of a single phase [$Ni_5(GeSn)_3$] with the same kinetic parameters ($K_0$, $D_0$, $E_k$, $E_d$) for all the experiments. The simulation allows reproducing the *in situ* XRD experimental points even if these points are scattered. Nemouchi *et al.*[66] have also determined the kinetic parameters of the $Ni_5Ge_3$ growth controlled by diffusion and reaction at the interface [Eqs. (2)–(4)] but considering the simultaneous growth of $Ni_5Ge_3$ and NiGe instead of the sequential growth of these two phases.

Table I summarizes the growth kinetic constants of the $Ni_5Ge_3$ and NiGe phases with or without Sn determined by simulations using either the parabolic model or linear-parabolic model, in comparison to those obtained by Nemouchi *et al.*[58] For the $Ni_5Ge_3$ phase, Nemouchi *et al.*[58] reported an activation energy of the diffusion ($E_d = 0.8$ eV) and that of the reaction ($E_k = 0.9$ eV) using a linear-parabolic simulation. The activation energy of the reaction and the diffusion for $Ni_5Ge_3$ is, respectively, 0.86 and 0.80 eV (Table I), which is in agreement with the reported studies.[58] The $E_k$ of $Ni_5(GeSn)_3$ is similar to that of $Ni_5Ge_3$. However, the activation energy of the diffusion of the $Ni_5(GeSn)_3$ phase is greater than that of $Ni_5Ge_3$. The value of $E_d$ is larger than that of $E_k$ in the $Ni_5(GeSn)_3$ phase, thus suggesting that diffusion is the limited mechanism during the growth of the $Ni_5(GeSn)_3$ phase. In the case of a parabolic simulation, the activation energy of the diffusion of the $Ni_5(GeSn)_3$ phase is greater than that of $Ni_5Ge_3$ (without Sn).

### D. $Ni_5(GeSn)_3$ phase relaxation

Figure 9 shows the evolution of the relative variation in the spacing between the crystallographic planes $\Delta d_\perp$ [Eq. (1)], (curve in red, right axis) during isothermal annealing at different temperatures, together with the evolution of the normalized diffraction intensity (left axis). All these *in situ* measurements show the same



**TABLE I.** Kinetic parameters of the normal growth of the $Ni_5(GeSn)_3$ and Ni(GeSn) phases obtained from all simulations carried out (isothermal and step). For $Ni_5Ge_3$ and NiGe, the values are taken from step annealing simulations and from Nemouchi *et al.*, respectively.

| Phase | Simulation | $K_0$ (cm/s) | $E_k$ (eV) | $D_0$ (cm²/s) | $E_d$ (eV) |
|---|---|---|---|---|---|
| $Ni_5Ge_3$[66] | Linear-Parabolic | 7 | 0.90 | $2 \times 10^{-6}$ | 0.80 |
| $Ni_5Ge_3$ | Linear-Parabolic | $6.8 \pm 1.3$ | $0.86 \pm 0.1$ | $1.9 \times 10^{-6} \pm 0.5 \times 10^{-6}$ | $0.80 \pm 0.06$ |
| $Ni_5(GeSn)_3$ | Linear-Parabolic | $20 \pm 5$ | $0.90 \pm 0.05$ | $0.25 \pm 0.10$ | $1.29 \pm 0.04$ |
| $Ni_5Ge_3$ | Parabolic | … | … | $2.9 \times 10^{-6} \pm 1.8 \times 10^{-6}$ | $0.84 \pm 0.06$ |
| $Ni_5(GeSn)_3$ | Parabolic | … | … | $1.6 \times 10^{-3} \pm 0.6 \times 10^{-3}$ | $1.12 \pm 0.02$ |
| NiGe[66] | Parabolic | … | … | $2 \times 10^{-6}$ | 0.90 |
| Ni–Ge | Parabolic | … | … | $2 \times 10^{-6} \pm 0.2 \times 10^{-6}$ | $0.93 \pm 0.01$ |
| Ni(GeSn) | Parabolic | … | … | $1.7 \times 10^{-3} \pm 0.6 \times 10^{-3}$ | $1.30 \pm 0.03$ |

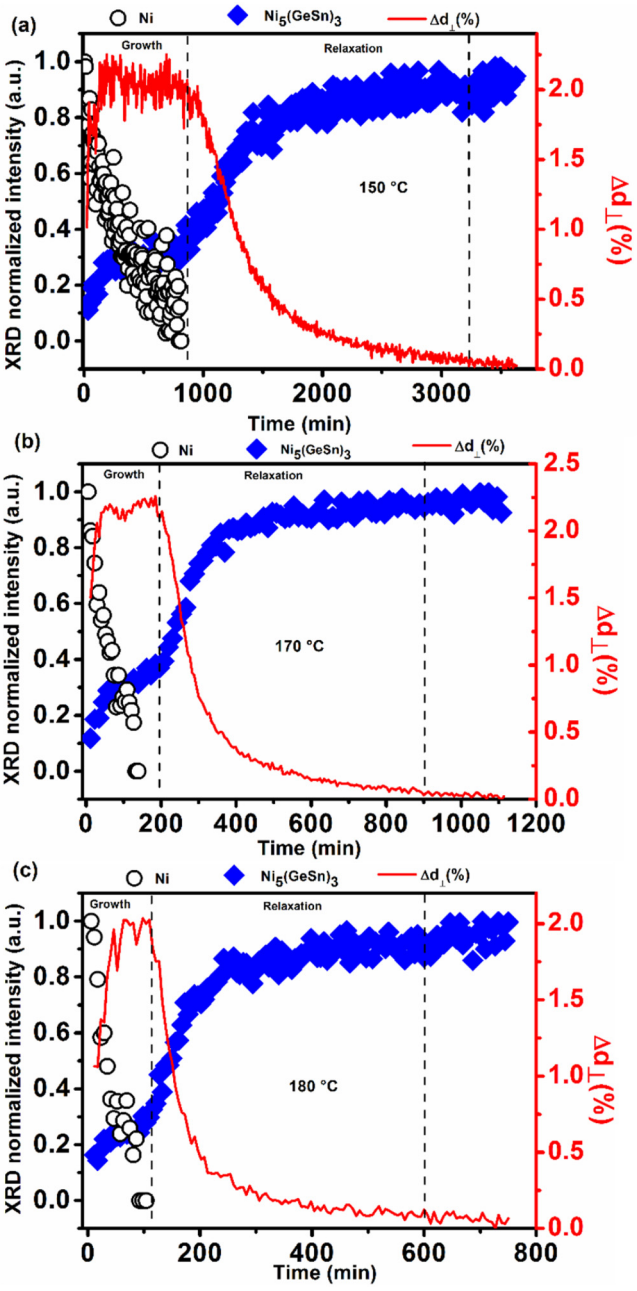


**FIG. 9.** The evolution of the normalized intensity of XRD peaks (left axis) and the relative variation of the interplanar spacing $\Delta d_{\perp}$ (right axis) during isothermal *in situ* XRD measurements at (a) 150, (b) 170, and (c) 180 °C.

behavior that was also observed during step annealing (Fig. 9). Indeed, after the total consumption of Ni (end of growth), a decrease in $\Delta d_{\perp}$ is observed for all experiments, characterizing a change in the lattice parameters of the $Ni_5(GeSn)_3$ phase (volume change). The change in the interplanar spacing can have several origins. When the temperature varies, it can be related to the thermal expansion of the material, but it cannot be the case for isothermal annealing during which the temperature is fixed. In the case of non-stoichiometric compounds, such as $Ni_5Ge_3$, this change can be related to a change in composition. However, a similar behavior has been observed when the first phase is stoichiometric and has been attributed to the creation and relaxation of stress induced by the change in volume during the reaction.[69–71] Since the change related to stress creation/relaxation is systematically observed (i.e., for stoichiometric and non-stoichiometric phases), the change in the lattice parameters of $Ni_5Ge_3$ is certainly due to the same mechanism. In the literature, the evolution of stress during the solid state reaction of a metal with a semiconductor has been the subject of several reviews.[71–73] Silicides are the most studied in this field.[72] The stress can have several origins (differences in thermal expansion, epitaxy, etc.), but, in the case of the formation of a new phase (reactive diffusion, oxidation, etc.), the main source of stress is the change in volume during the reaction, which is expressed by the Pillings–Bedworth ratio,[72]

$$\frac{\Delta V}{V} = \frac{V(A_pB_q) - V(B)}{V(B)}. \tag{5}$$

Equation (5) is valid if $A$ is the element, which mainly diffuses [if $B$ mainly diffuses $V$ ($A$) must replace $V$ ($B$)]. Generally, the volume of the formed phase is greater than the volume consumed (positive Pillings–Bedworth ratio), which leads to compressive stress. Zhang and d'Heurle[72] have proposed a model that explains qualitatively the origin and evolution of stress. It is based on the distinction between the stress generation resulting from the growth, which is controlled by the diffusion of the fast-moving atoms, and the stress relaxation controlled by the diffusion of the slow moving atoms. A qualitative agreement was obtained between the model and the experiments for the formation of $Pd_2Si$.[72] The same qualitative behavior as in Fig. 9 is observed, suggesting that the change in lattice parameters in the $Ni_5(GeSn)_3$ phase is due to stress evolution. This behavior is in accordance with former observations[69,74–76] and with the model proposed by Zhang and d'Heurle.[72] In this model, the generation of stress due to the change in volume is concomitant with the relaxation of the stresses during the growth while only the stress relaxation takes place when the growth is finished (i.e., after total consumption of the metal).[60]

### E. Initiation of Ni(GeSn) phase formation

Table II shows the stability temperatures of the different phases from *in situ* XRD measurements for the Ni–Ge and $Ni–Ge_{0.9}Sn_{0.1}$ systems. The temperature for which the Ni-rich phase is fully consumed is higher (about 40 °C) in the case of the $Ni–Ge_{0.9}Sn_{0.1}$ system. The same phenomenon was observed by Quintero *et al.*[56] for the same system ($Ni–Ge_{0.9}Sn_{0.1}$), but these authors found a larger shift in the total consumption temperature of the Ni-rich phase (around 60 °C) compared to the Ni–Ge system. Table II shows that the thermal stability of the $Ni_5(GeSn)_3$ phase is higher than the one of the $Ni_5Ge_3$ phase. Therefore, the addition of Sn in the $Ni_5Ge_3$ phase increases its thermal stability.

**TABLE II.** Stability temperatures of the different phases from *in situ* XRD measurements for the Ni–Ge and Ni–$Ge_{0.9}Sn_{0.10}$ systems.

| Phase | $Ni_5Ge_3$ | $Ni_5(GeSn)_3$ | NiGe | Ni(GeSn) |
|---|---|---|---|---|
| Temperature (°C) | 120–250 | 120–290 | 205–545 | 275–430 |

Consequently, the formation of the Ni(GeSn) phase, the low resistive phase, is delayed. This delay can be explained by a nucleation difficulty of the Ni(GeSn) phase at the $Ni_5(GeSn)_3/Ge_{0.9}Sn_{0.1}$ interface that induces an incubation time. However, the delay observed before the formation of Ni(GeSn) is more probably linked to the stress relaxation since the formation of Ni(GeSn) is observed when the stress is relaxed (Fig. 9). Indeed, in the case of the Ni–Si system, Mangelinck *et al.*[65] have also observed a delay between the end of δ-$Ni_2Si$ growth and the start of NiSi formation that was found to follow an Arrhenius behavior. This delay was related to stress relaxation in the δ-$Ni_2Si$ phase.[65] It was found that the growth of NiSi only occurs when the stress relaxation in the δ-$Ni_2Si$ is finished.[65] A similar behavior could be the cause of the delay between $Ni_5(GeSn)_3$ and Ni(GeSn) since a large stress relaxation is observed for $Ni_5(GeSn)_3$ during this delay.

Therefore, two mechanisms may control the initiation of NiGeSn phase formation: nucleation or stress relaxation in $Ni_5Ge_3$. Sn can impact both mechanisms. Regarding nucleation, it has been shown that the entropy effect induced by an alloy element can significantly affect nucleation.[63,77] If the alloyed element is less soluble in the phase to be nucleated than in the phase(s) being consumed, the driving force for nucleation may be significantly reduced, leading to a substantial increase in the nucleation temperature.[63,77] Since Sn is fully soluble in $Ni_5Ge_3$ but almost insoluble in NiGe, the addition of Sn in Ge should increase the nucleation temperature of NiGe.

However, as discussed above, the delay in the formation of NiGe with Sn is more likely due to stress relaxation in $Ni_5Ge_3$. This stress relaxation is believed to be controlled by the diffusion of the less mobile species, which is likely Ge in $Ni_5Ge_3$. Our results clearly show that Sn slows down stress relaxation in $Ni_5Ge_3$. This is certainly related to a slowdown of Ge diffusion in the presence of Sn, which ultimately delays the formation of NiGe.

According to Table II, the stability of the Ni(GeSn) phase at high temperature is lower than that of the NiGe phase. This is due certainly to the rejection of Sn from Ni(GeSn) at high temperature. This last phenomenon will be discussed later.

### F. Ni(GeSn) growth kinetics

In order to determine the kinetic parameters of the Ni(GeSn) phase growth, *in situ* XRD annealing by step [Fig. 2(b)] as well as the isothermal annealing (Fig. 7) were simulated with the diffusion controlled growth model [Eq. (2) was used but with a very low value of $K$ in order to have a diffusion controlled growth].

Figure 10 summarizes the simulations carried out by considering that only one phase is formed and by using the same kinetic parameters ($D_0$, $E_d$) for the simulations of all the experiments.

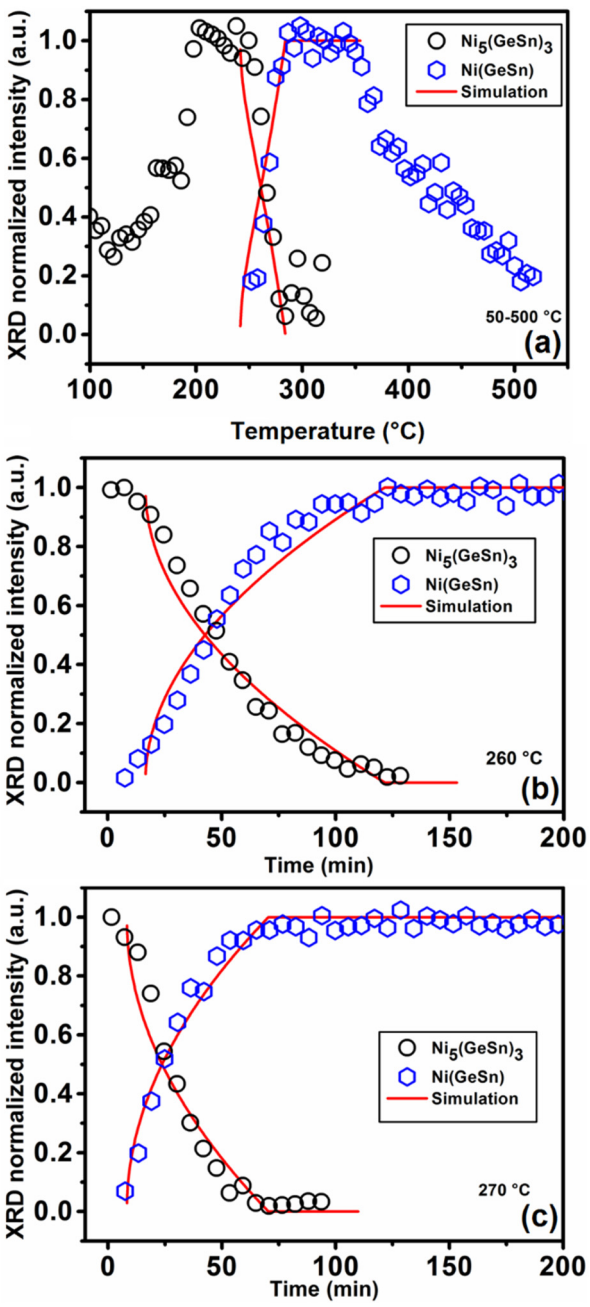


**FIG. 10.** Simulation of growth of the Ni(GeSn) phase using *in situ* XRD experiments carried out for the Ni–$Ge_{0.9}Sn_{0.10}$ system: (a) by step, (b) isothermal at $T = 260$ °C, and (c) isothermal at $T = 270$ °C.

Overall, the experimental results and the simulated curves are in good agreement. This means that all the annealing can be simulated with the same kinetic parameters, considering the formation of only one Ni(GeSn) phase.

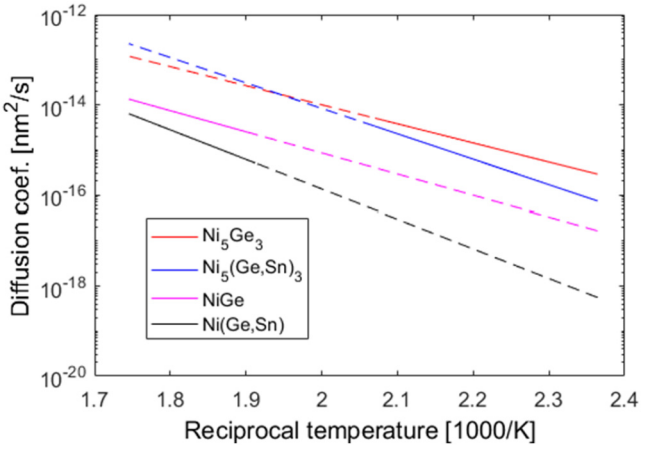


**FIG. 11.** Arrhenius plot of the diffusion coefficient obtained from the diffusion-controlled growth model. The solid line corresponds to the temperature range for which the fits were performed while the dashed line included the full range of growth temperature.

Table I summarizes the values of the kinetic constants of the normal growth of Ni(GeSn) obtained in this work and compares them with those obtained by Nemouchi *et al.*[66] for NiGe. The pre-exponential coefficient $D_0$ and the diffusion activation energy $E_d$ for NiGe are lower than those of the Ni(GeSn). For NiGe without Sn, the kinetic parameters, $D_0$ and $E_d$, obtained in our work are similar to the ones obtained by Nemouchi *et al.*[66] The higher activation energy for diffusion in Ni(GeSn) than in NiGe indicates that Sn slows down the diffusion in NiGe.

In order to compare these diffusion coefficients, an Arrhenius plot is shown in Fig. 11 for the diffusion coefficients obtained from the diffusion-controlled growth model.

As mentioned before, the growth of stanogermanides [Ni(GeSn), $Ni_5(GeSn)_3$] in thin films is expected to be controlled by Ni diffusion that is the fast diffusing species in these phases as well as in the germanide ($Ni_5Ge_3$ and NiGe) and in the silicide ($Ni_2Si$ and NiSi).[63] For silicides that have been extendedly studied, it was observed that metal diffusion is faster in metal-rich silicides (and, reciprocally, Si diffusion is faster in Si-rich silicides).[78] This rule has been called the "$Cu_3Au$" rule by d'Heurle *et al.*[78] and explained by the fact that in a phase that is richer in one element (metal), this element can diffuse on its own sublattice (metal sublattice) and does need to pass on the other element (Si) sublattice (as antisite defect). Such a diffusion of a element on its own lattice costs less energy resulting in a lower diffusion activation energy. Therefore, our measurement of a lower activation energies for $Ni_5(GeSn)_3$ than for NiGeSn is in accordance with the "$Cu_3Au$" rule.

Our results show also that the presence of Sn slows down the diffusion in $Ni_5Ge_3$ and in NiGe by decreasing the diffusion activation energy. Again, one may refer to the silicide literature to explain this behavior. Indeed, the effect of alloy element on the silicide formation in thin films has been widely studied,[63,79,80] and it was shown that several alloy elements such as Pt, W, ettc. can slow down the formation of the Ni silicide phase.[63,80] This was attributed to segregation of the alloy element to the grain boundary of the growing silicide.[63] As, in thin films, the diffusion mainly occurs at the grain boundaries because the grain are very small, the segregation of the alloy element at GB can, thus, have an effect on the diffusion coefficient and increase the diffusion activation energy.

The microstructure of the Ge or Ge(Sn) layer may also affect the time for growth completion through a change in the microstructure of the stanogermanide such as the grain size that have a direct impact on the diffusion coefficient in the germanide. However, the Ge and Ge(Sn) layers are both in epitaxy (Fig. 1): therefore, no large difference in their microstructure is expected, and this small difference should not influence the microstructure and growth of the intermetallics.

The Arrhenius plot in Fig. 11 shows an interesting crossover between the diffusion coefficients of $Ni_5Ge_3$ and $Ni_5(GeSn)_3$ around 200 °C. This indicates that at this temperature, the diffusion rates in both intermetallics are equal. This behavior can be explained by the fact that the addition of Sn reduces the diffusion coefficient of $Ni_5(GeSn)_3$ compared to $Ni_5Ge_3$. However, as the temperature increases, the diffusion coefficient of $Ni_5(GeSn)_3$ increases more rapidly than that of $Ni_5Ge_3$, leading to a crossover point around 200 °C where both diffusion coefficients are equal. The crossover point has important implications for the growth behavior of the intermetallics. In particular, it explains why the completion temperatures for growth in $Ni_5Ge_3$ and $Ni_5(GeSn)_3$ are close when using step annealing. Since the diffusion rates in both intermetallics are equal at around 200 °C, the time and temperature required for growth completion are similar for both $Ni_5Ge_3$ and $Ni_5(GeSn)_3$, despite the differences in their diffusion coefficients at other temperatures at which the isothermal annealing was performed.

Overall, the Arrhenius plot in Fig. 11 provides valuable insights into the diffusion behavior of $Ni_5Ge_3$ and $Ni_5(GeSn)_3$ and its impact on the growth kinetics of these intermetallics. Indeed, the growth of an intermetallic compound is primarily determined by the diffusion within the compound itself. Therefore, the time (or temperature) it takes for the intermetallic to grow is dependent on the thickness of the growing intermetallic ($Ni_5Ge_3$ and NiGe). More precisely, in the case of diffusion-controlled growth during isothermal annealing, the time required to fully form the intermetallic is proportional to the square of the maximum thickness of the intermetallic and inversely proportional to its diffusion coefficient. For reaction–diffusion growth, the dependencies are more complex since both the reaction rate and the diffusion coefficient play a role in determining the growth kinetics. Furthermore, the maximum intermetallic thickness is proportional to the thickness of the metal (i.e., $L_{NiGe} = 2\ l_{Ni}$) since the amount of metal is limited compared to the amount of semiconductor. Therefore, the time (or temperature) for the growth completion depends on the Ni thickness but not on the thickness of the Ge or Ge(Sn) layers.

Understanding the diffusion behavior of $Ni_5Ge_3$ and $Ni_5(GeSn)_3$ and its impact on the growth kinetics of these intermetallics is important for optimizing the growth conditions and achieving high-quality intermetallic layers for various applications.

When the final intermetallic, NiGe, is fully formed, no further phase growth occurs since NiGe is in equilibrium with Ge, as

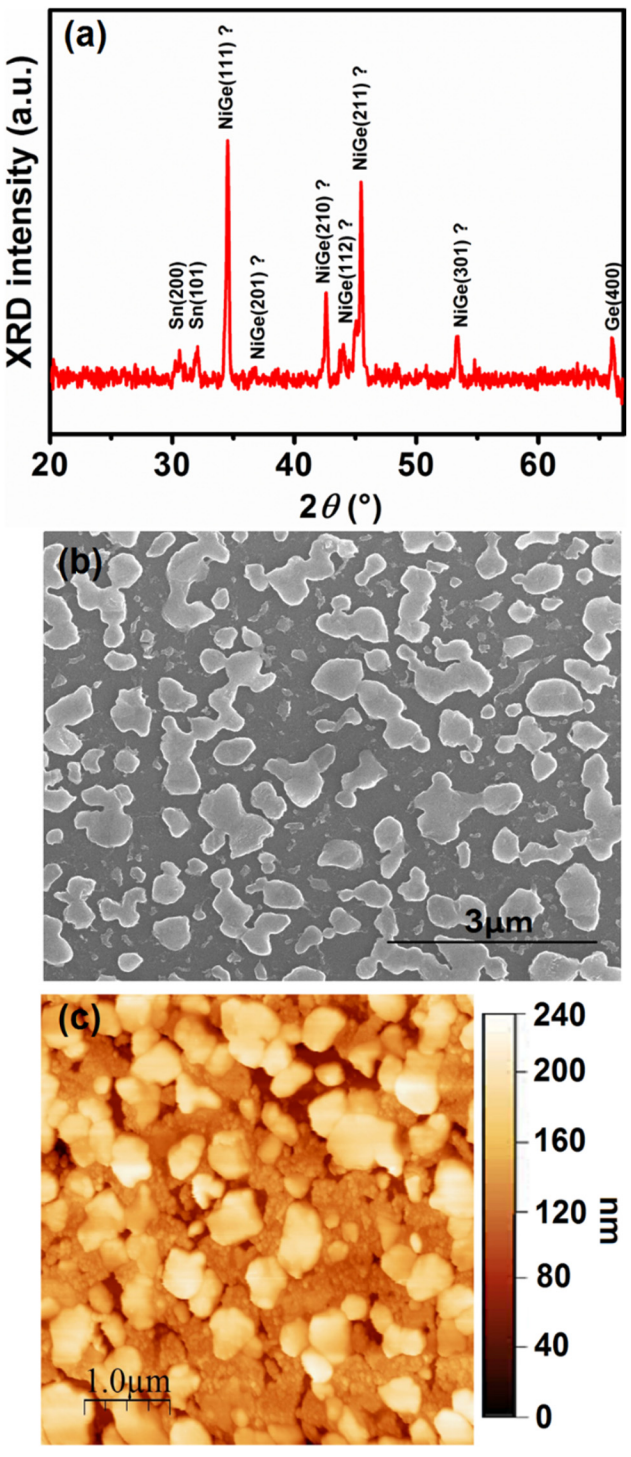


**FIG. 12.** Analyses carried out at room temperature on the Ni–GeSn sample after the *in situ* annealing presented in Fig. 2(b) (step annealing): (a) x-ray diffractogram, (b) SEM surface measurements, and (c) AFM surface measurements.

indicated by the green cross in Fig. 5. However, morphological changes such as agglomeration can still occur. For the Ni–Ge(10% Sn) system, in addition to agglomeration, Sn can be rejected from NiGe and from Ge(Sn) in order to reach the three-phase equilibrium (NiGe, Ge, and Sn), as indicated by the blue cross in the ternary phase diagram (Fig. 5). This rejection of Sn lead to the formation of Sn-rich precipitates, which can impact the overall properties of the contact and the Ge(Sn) layer and will be discussed now.

### G. Sn segregation kinetics

Figure 12(a) shows the diffractogram measured at room temperature on the sample presented in Fig. 1(b) after step annealing. XRD peaks corresponding to β-Sn are detected and should result from the crystallization of liquid Sn (the melting temperature of Sn is 232 °C),[81] which was rejected at high temperature from the Ni(GeSn) and $Ge_{0.9}Sn_{0.1}$ phase. The positions of the XRD peaks

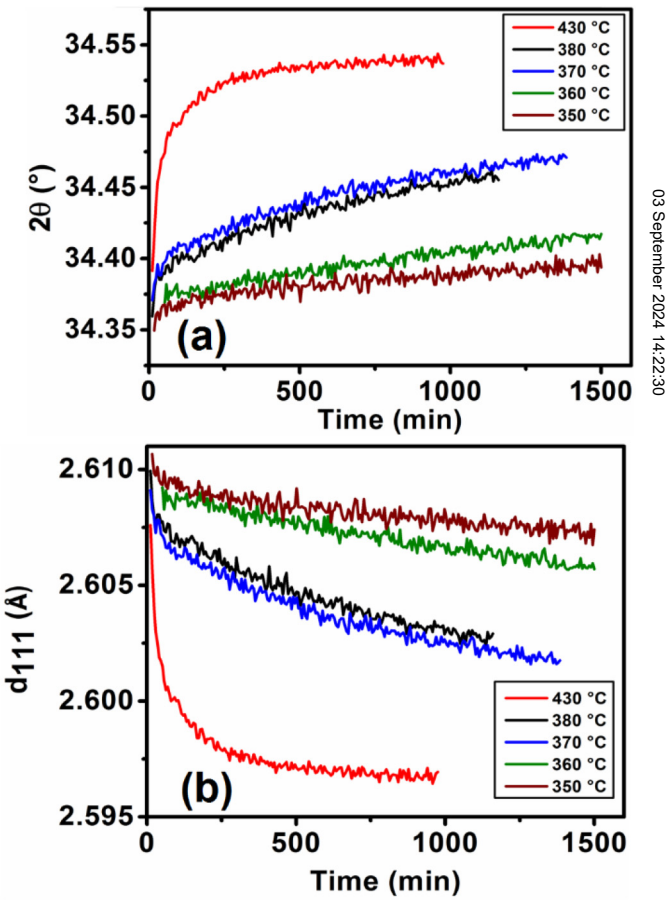


**FIG. 13.** Variation in (a) angular position $2\theta$ and (b) interplanar spacing $d_{111}$ for the crystallographic (111) plane of the Ni(GeSn) phase vs time during isothermal annealing at different temperatures (350, 360, 370, 380, and 430 °C).

for the Ni(GeSn) phase correspond to the angular positions of NiGe. This indicates that the rejection of Sn from the Ni(GeSn) phase leads to the NiGe phase without Sn. Figure 12(b) presents a surface SEM image of this sample. Large islands are observed with a lateral size between 0.1 and 2 $\mu$m. These islands are also observed on the AFM image [Fig. 12(c)]. They have heights between 115 and 170 nm, significantly greater than the thickness of the Ni(GeSn) layer. The average surface roughness (RMS) is about 38 nm. These islands probably correspond to the Sn-rich phase that was crystallized during cooling and/or to the agglomeration of the Ni monogermanide. The NiGe/Sn phase separation and NiGe phase agglomeration lead, thus, to deterioration of film morphology. The thermal stability of the NiGe phase is, therefore, considerably affected by the incorporation of Sn. The variation in the diffraction angle $2\theta$ and the interplanar spacing $d_{111}$ (determined from Brag's law) of the Ni(GeSn) phase, as a function of time during isothermal annealing at different temperatures, are presented in Fig. 11.

The variation in the (111) XRD peak position $2\theta$ and the interplanar spacing $d_{111}$ of the Ni(GeSn) phase over time is shown in Fig. 13. This evolution occurs during isothermal annealing at various temperatures: 350, 360, 370, 380, and 430 °C. The interplanar spacing $d_{111}$ (and inversely the angle $2\theta$) decreases with time, which indicates a decrease in the volume of Ni(GeSn). Since the stress relaxation is generally small for the second phases compared to the first phases, it should not explain the large change in $d_{111}$. Moreover, XRD, SEM, and AFM measurements of the samples after step annealing show that Sn is rejected from NiGe (Fig. 12). This decrease can be, thus, interpreted by the rejection of Sn from Ni(GeSn) since the incorporation of Sn into NiGe is expected to increase its volume. The initial values of $d_{111}$ are approximately similar for the different temperature and should correspond to the 10% of Sn introduced during the deposition of $Ge_{0.9}Sn_{0.1}$. The change in $d_{111}$ [Fig. 13(b)] is faster when the temperature increases (the isotherms at 370 and 380 °C appear to be reversed, but this may be due to a global shift related to a misalignment of the sample). This means that the rejection of Sn increases with temperature and is, thus, thermally activated. In order to determine the Sn segregation kinetics from the *in situ* XRD, we performed simulations considering that the segregation kinetics is controlled by the diffusion of Sn through the Ni(GeSn) film toward the surface to form a film of pure Sn (Fig. 12). Indeed, the rejection of Sn occurs certainly from the bulk of NiGe to the surface and can be assimilated to a surface segregation.

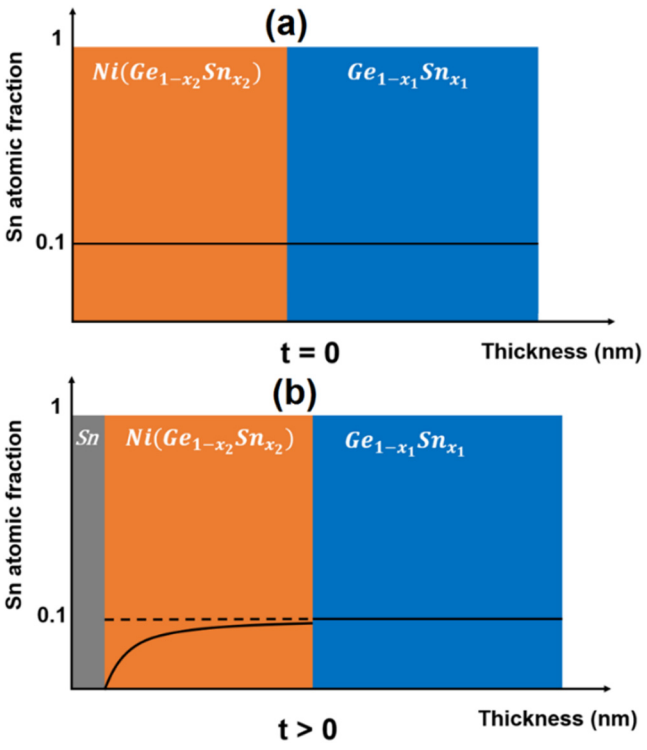


**FIG. 14.** Schematic illustration of the Sn content profile in the Ni(GeSn) phase as a function of the thickness at (a) $t = 0$ and (b) $t > 0$.

As a first approximation, we considered that the diffusion of Sn in the Ni(GeSn) phase takes place with an effective diffusion coefficient, $D_{\text{eff}}$, that should be mainly related to grain boundary diffusion since the Ni(GeSn) film is polycrystalline. The diffusion of Sn in Ge(Sn) was considered as negligible.[82] From these approximations, the diffusion of Sn in Ni(GeSn) was simulated by one-dimensional finite differences based on Fick's law with the diffusion coefficient $D_{\text{eff}}$. As an initial condition ($t = 0$), the Sn atomic fraction was taken as constant within the Ni(GeSn) film and equal to 10% [Fig. 14(a)]. The Sn atomic fraction in NiGe at the Sn/NiGe interface was considered as null for all the time ($t > 0$) as shown in Fig. 14(b).

For each time step, a Sn concentration profile is obtained and depends on the diffusion coefficient used to perform the simulation. This concentration profile is averaged over the Ni(GeSn) layer in order to compare with the XRD intensity. Indeed, in the case of a layer with a non-uniform composition, the position of the XRD peak only provide an average value of the interplanar spacing through Bragg's law. From this spacing, a global information on the average composition of the Ni(GeSn) layer can be obtained from Vegard's law (i.e., linear variation in the lattice parameters of NiGe with the Sn concentration). For the *in situ* XRD measurements, the average composition was determined from the (111) XRD peak, by assuming that the minimum ($2\theta \sim 34.35° \rightarrow d_{111} \sim 0.261$ nm) corresponds to 10% Sn and the maximum ($2\theta \sim 35.55° \rightarrow d_{111} = 0.252$ nm) to 0%. These average compositions (curve in red) determined from *in situ* XRD are compared to the average concentration obtained from the simulated Sn profile in Ni(GeSn) (curve in blue) in Fig. 15. The simulated curves were fitted to the experimental ones by changing the effective diffusion coefficients.

In general, the experimental and the simulated curves are in good agreement indicating that the proposed model allows us to reproduce the kinetics of Sn segregation. There is a shift between the experimental and the simulated curve for the isotherm at $T = 370°$ [Fig. 15(c)] that could be linked to a systematic shift of $2\theta$ during this experiment. Our simulations allow the determination of the effective diffusion coefficients of Sn for each temperature.

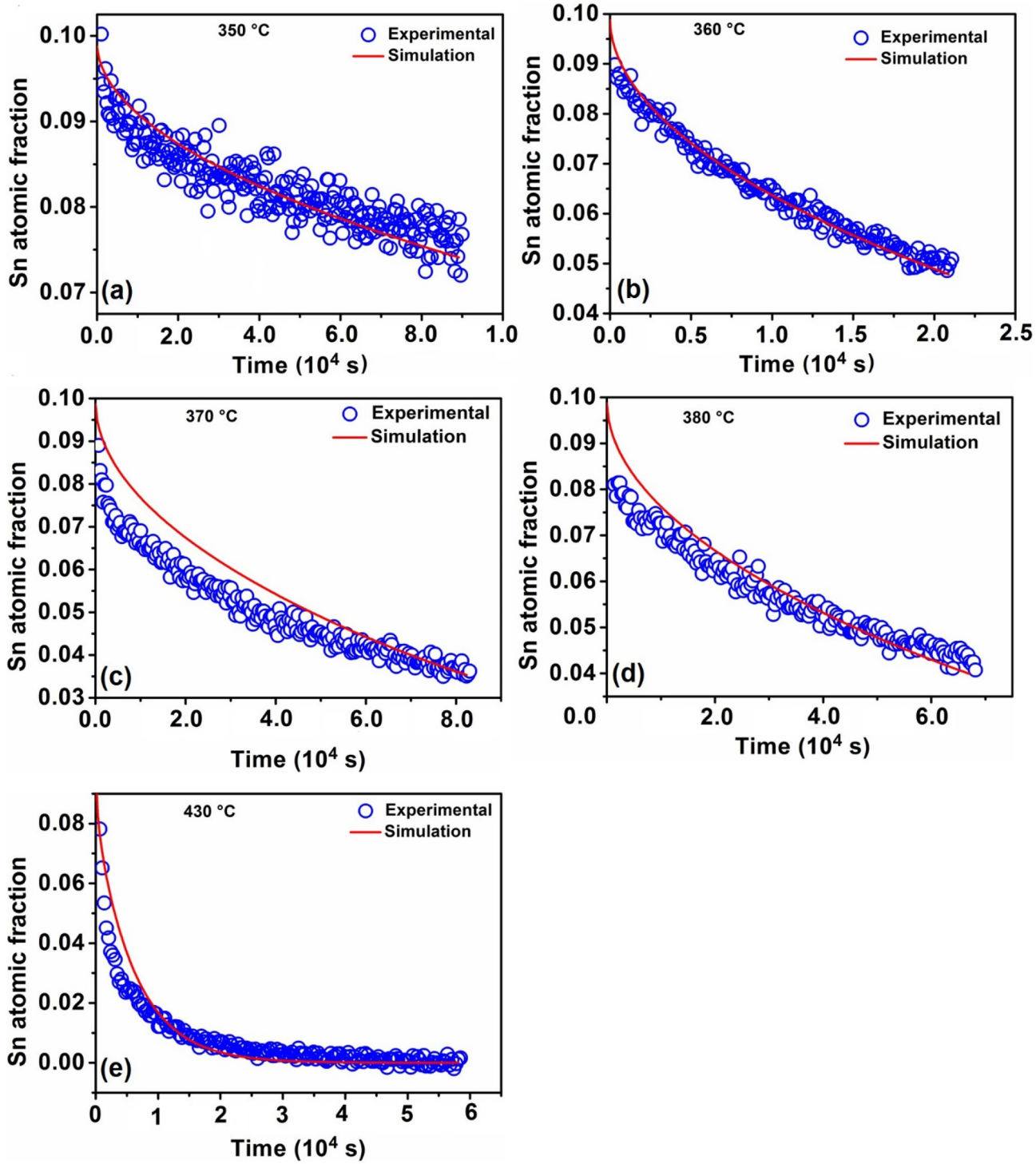


**FIG. 15.** Sn concentration variation in Ni(GeSn) phase as a function of time (blue circles) and their fit (red curve) determined from isothermal *in situ* XRD measurements at (a) $T = 350$ °C, (b) $T = 360°$, (c) $T = 370$ °C, (d) $T = 380$ °C, and (e) $T = 430$ °C. The fit (red curve) has been obtained by changing the effective diffusion coefficient in the model described in the text.

**TABLE III.** Summary of the effective diffusion coefficient $D_{eff}$ ($nm^2/s$) values at different *in situ* XRD temperatures.

| Temperature (°C) | $D_{eff}$ ($nm^2/s$) |
|---|---|
| 350 | $9.0 \times 10^{-4}$ |
| 360 | $1.6 \times 10^{-3}$ |
| 370 | $6.4 \times 10^{-3}$ |
| 380 | $6.7 \times 10^{-3}$ |
| 430 | $1.0 \times 10^{-1}$ |

Table III summarizes the values of the diffusion coefficient $D_{eff}$ for different isothermal annealing. An increase in the diffusion coefficient with increasing temperature shows that the rate of Sn segregation is thermally activated. In the case of a diffusion that is carried out by a unique mechanism in the same temperature range, the diffusion coefficient $D$ follows an Arrhenius law:

$$D = D_0 \exp\left(-\frac{E_a}{kT}\right), \tag{6}$$

with $D_0$ being the pre-exponential factor and $E_a$ being the activation energy.

In order to determine the activation energy of Sn segregation, the variation in the effective diffusion coefficient of Sn as a function of $1/T$ is plotted in the Arrhenius diagram of Fig. 14.

From this Arrhenius diagram, an activation energy for Sn diffusion in the Ni(GeSn) phase, $E_a = 2.91$ eV, and a pre-exponential factor, $D_0 = 1.94.10^3$ $cm^2/s$, are obtained to give the following expression:

$$D = 1.94 \times 10^3 \exp\left(-\frac{2.91\ \text{eV}}{kT}\right)\ \text{cm}^2\text{s}^{-1}. \tag{7}$$

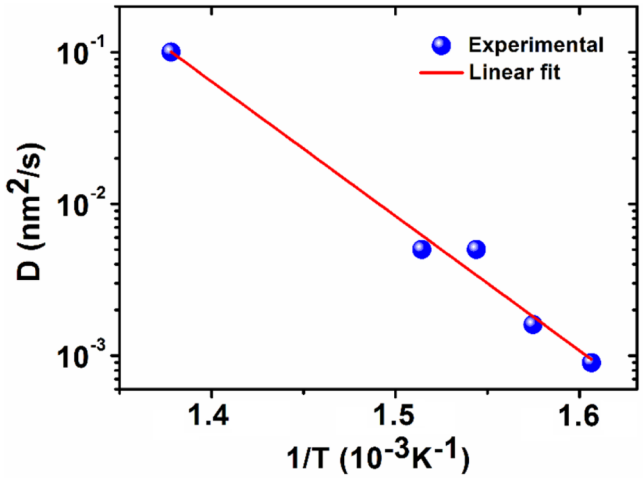


**FIG. 16.** Arrhenius diagram of the effective diffusion coefficients of Sn in the Ni(GeSn) phase.

This activation energy is close to the one for the diffusion of Sn in Ge (3 eV).[83] The similarity between these activation energies suggests that Sn probably diffuses in the Ge sub-lattice in the NiGe phase. The good agreement between the simulations and the experiments indicates that the model and its approximations are realistic. However, the Ni(GeSn) film is polycrystalline, and both the diffusion at the grain boundaries and the diffusion in the grains must contribute to the Sn segregation. The Arrhenius behavior observed in Fig. 16 indicates that segregation can be described by an effective diffusion coefficient. Since the grain size usually scales with the thickness of the film, a significant contribution of the grain boundary diffusion is expected. However, as XRD is sensitive to the lattice spacing and, thus, to the concentration of Sn inside the NiGe grains, the lattice diffusion should also contribute to the effective diffusion.

### H. Electrical properties

Now that we have established the kinetics of formation and degradation, and it serves as a foundation for optimizing the process for contacts. However, it is equally important to consider another critical parameter for contacts: sheet resistance. *In situ* four-point sheet resistance measurements ($R_{sh}$) have been performed on the Ni–$Ge_{1-x}Sn$ sample. The results indicate that the $R_{sh}$ of the $Ni_5(GeSn)_3$ phase can reach approximately 49 Ω/sq at 200 °C. However, at about 300 °C, the sheet resistance for the Ni(GeSn) phase falls to about 17 Ω/sq. This significant reduction in $R_{sh}$ by a factor of three confirms that the Ni(GeSn) phase is the least resistive and, therefore, the most promising for microelectronic applications.

A measurement of the four-point sheet resistance at room temperature was carried out on the NiGeSn phase after rapid thermal annealing (RTA) at 300 °C for 2 min. A value of 6 ohms/square was obtained, which is five times lower than that reported by Quintero *et al.*[84] (~30 Ω/sq) for the NiGeSn and NiGe phases. This sheet resistance is comparable to that of the NiSi phase,[85] which is widely used in microelectronics. These results suggest that the NiGeSn phase is an excellent candidate for forming ohmic contacts in microelectronic devices.

## V. CONCLUSIONS

The solid-state reaction of the Ni film with epitaxial Ge or $Ge_{0.9}Sn_{0.1}$ film produced by magnetron sputtering on Si (100) has been studied. For both systems, the sequential formation of two phases, the hexagonal Ni-rich phase [$Ni_5Ge_3$ and $Ni_5(GeSn)_3$] and the orthorhombic phase [NiGe and Ni(GeSn)], is observed, and the phase sequence is, thus, not changed by the presence of Sn. However, the germination and growth kinetics of Ni germanides are modified by the addition of Sn.

Two regimes are observed for the $Ni_5(GeSn)_3$ phase. One corresponds to the growth of the phase by consuming the Ni film, and the other corresponds to a variation in the lattice parameters of the

phase after the consumption of the Ni layer. We have shown qualitatively that the variation in the lattice parameters is probably related to the stress relaxation in the $Ni_5(GeSn)_3$ phase.

The simulations using a reaction/diffusion controlled growth model of the *in situ* XRD measurements allowed us to determine the parameters for the growth kinetic of the stanogermaniures. The growth kinetics of $Ni_5(GeSn)_3$ and Ni(GeSn) are primarily controlled by the diffusion of Ni, but the presence of Sn slows down this diffusion through these phases.

The *in situ* XRD measurements also shows a delay in the formation of Ni(GeSn) phase. The delayed growth of Ni(GeSn) only occurs when the stress relaxation in the $Ni_5(GeSn)_3$ is finished. This delay leads to the formation of the Ni(GeSn) phase at a higher temperature than for the NiGe phase. The thermal stability of the NiGe phase is strongly affected by the presence of Sn, causing NiGe/Sn phase separation and agglomeration of the NiGe phase. Indeed, at high temperature, Sn can diffuse to the surface. Based on experimental data and simulations, we determined an effective diffusion coefficient and its temperature variation corresponding to the Sn segregation out of the Ni(GeSn) phase. The kinetic parameters obtained make it possible to predict the behavior of Sn during the fabrication by reactive diffusion of Ni stanogermanides and during the thermal degradation of NiGe.

## ACKNOWLEDGMENTS

This work was supported by the French-Algerian cooperation program PROFAS B+. Anders Hallén from the Ion Technology Centre ITC, Uppsala University, Sweden, is acknowledged for the RBS measurements. Drisse Hannani, CNRS engineer, IM2NP Marseille, is acknowledged for the AFM facilities.

## AUTHOR DECLARATIONS

### Conflict of Interest

The authors have no conflicts to disclose.

### Author Contributions

**H. Khelidj:** Conceptualization (equal); Data curation (equal); Formal analysis (equal); Funding acquisition (equal); Investigation (equal); Methodology (equal); Software (equal); Visualization (equal); Writing – original draft (equal). **A. Portavoce:** Conceptualization (equal); Formal analysis (equal); Methodology (equal); Project administration (equal); Resources (equal); Software (equal); Supervision (equal); Validation (equal); Writing – review & editing (equal). **K. Hoummada:** Conceptualization (equal); Project administration (equal); Supervision (equal); Validation (equal); Visualization (equal); Writing – review & editing (equal). **M. Bertoglio:** Methodology (equal); Resources (equal); Visualization (equal). **M. C. Benoudia:** Methodology (equal); Resources (equal); Supervision (equal). **M. Descoins:** Methodology (equal); Resources (equal); Visualization (equal). **D. Mangelinck:** Conceptualization (equal); Formal analysis (equal); Methodology (equal); Project administration (equal); Software (equal); Supervision (equal); Validation (equal); Visualization (equal); Writing – review & editing (equal).

## DATA AVAILABILITY

The data that support the findings of this study are available from the corresponding author upon reasonable request.

## REFERENCES

[1]C. Rogers, A. Y. Piggott, D. J. Thomson, R. F. Wiser, I. E. Opris, S. A. Fortune, A. J. Compston, A. Gondarenko, F. Meng, X. Chen, G. T. Reed, and R. Nicolaescu, "A universal 3D imaging sensor on a silicon photonics platform," Nature **590**, 256–261 (2021).
[2]F. P. Sunny, E. Taheri, M. Nikdast, and S. Pasricha, "A survey on silicon photonics for deep learning," ACM J. Emerg. Technol. Comput. Syst. **17**, 1–57 (2021).
[3]D. Thomson, A. Zilkie, J. E. Bowers, T. Komljenovic, G. T. Reed, L. Vivien, D. Marris-Morini, E. Cassan, L. Virot, J.-M. Fédéli, J.-M. Hartmann, J. H. Schmid, D.-X. Xu, F. Boeuf, P. O'Brien, G. Z. Mashanovich, and M. Nedeljkovic, "Roadmap on silicon photonics," J. Opt. **18**, 073003 (2016).
[4]S. Al-Kabi, S. A. Ghetmiri, J. Margetis, T. Pham, Y. Zhou, W. Dou, B. Collier, R. Quinde, W. Du, A. Mosleh, J. Liu, G. Sun, R. A. Soref, J. Tolle, B. Li, M. Mortazavi, H. A. Naseem, and S.-Q. Yu, "An optically pumped 2.5 $\mu$m GeSn laser on Si operating at 110 K," Appl. Phys. Lett. **109**, 171105 (2016).
[5]T. Nagatsuma, G. Ducournau, and C. C. Renaud, "Advances in terahertz communications accelerated by photonics," Nat. Photon. **10**, 371–379 (2016).
[6]M. Cazzanelli, F. Bianco, E. Borga, G. Pucker, M. Ghulinyan, E. Degoli, E. Luppi, V. Véniard, S. Ossicini, D. Modotto, S. Wabnitz, R. Pierobon, and L. Pavesi, "Second-harmonic generation in silicon waveguides strained by silicon nitride," Nat. Mater. **11**, 148–154 (2012).
[7]C. Lacava, S. Stankovic, A. Z. Khokhar, T. D. Bucio, F. Y. Gardes, G. T. Reed, D. J. Richardson, and P. Petropoulos, "Si-rich silicon nitride for nonlinear signal processing applications," Sci. Rep. **7**, 22 (2017).
[8]Y. Kim, M. Takenaka, T. Osada, M. Hata, and S. Takagi, "Strain-induced enhancement of plasma dispersion effect and free-carrier absorption in SiGe optical modulators," Sci. Rep. **4**, 4683 (2014).
[9]J. Michel, J. Liu, and L. C. Kimerling, "High-performance Ge–on–Si photodetectors," Nat. Photon. **4**, 527–534 (2010).
[10]I. Stavarache, C. Logofatu, M. T. Sultan, A. Manolescu, H. G. Svavarsson, V. S. Teodorescu, and M. L. Ciurea, "SiGe nanocrystals in $SiO_2$ with high photosensitivity from visible to short-wave infrared," Sci. Rep. **10**, 3252 (2020).
[11]F. Boeuf, S. Cremer, E. Temporiti, M. Fere, M. Shaw, N. Vulliet, B. Orlando, D. Ristoiu, A. Farcy, T. Pinguet, A. Mekis, G. Masini, P. Sun, Y. Chi, H. Petiton, S. Jan, J. R. Manouvrier, C. Baudot, P. L. Maitre, J.-F. Carpentier, L. Salager, M. Traldi, L. Maggi, D. Rigamonti, C. Zaccherini, C. Elemi, B. Sautreuil, and L. Verga, "Recent progress in silicon photonics R&D and manufacturing on 300 mm wafer platform," in *Optical Fiber Communication Conference (2015)* (Optical Society of America, 2015), p. W3A.1.
[12]D. Feng, B. J. Luff, S. Jatar, and M. Asghari, "Micron-scale silicon photonic devices and circuits," in *Optical Fiber Communication Conference (2014)* (Optical Society of America, 2014), p. Th4C.1.
[13]C. Doerr, L. Chen, D. Vermeulen, T. Nielsen, S. Azemati, S. Stulz, G. McBrien, X.-M. Xu, B. Mikkelsen, M. Givehchi, C. Rasmussen, and S.-Y. Park, "Single-chip silicon photonics 100 Gb/s coherent transceiver," in *Optical Fiber Communication Conference: Postdeadline Papers (2014)* (Optical Society of America, 2014), p. Th5C.1,
[14]A. H. Ahmed, A. Sharkia, B. Casper, S. Mirabbasi, and S. Shekhar, "Silicon-photonics microring links for datacenters—Challenges and opportunities," IEEE J. Sel. Top. Quantum Electron. **22**, 194–203 (2016).
[15]See https://pubs.aip.org/aip/app/article/7/2/020902/2835121/Scaling-up-silicon-photonic-based-accelerators for "Scaling up silicon photonic-based accelerators: Challenges and opportunities" (accessed 26 May 2023).
[16]R. People and J. C. Bean, "Calculation of critical layer thickness versus lattice mismatch for $Ge_xSi_{1-x}$/Si strained-layer heterostructures," Appl. Phys. Lett. **47**, 322–324 (1985).

[17]J. W. Matthews and A. E. Blakeslee, "Defects in epitaxial multilayers," J. Cryst. Growth **27**, 118–125 (1974).
[18]S. An, H. Park, and M. Kim, "Recent advances in single crystal narrow band-gap semiconductor nanomembranes and their flexible optoelectronic device applications: Ge, GeSn, InGaAs, and 2D materials," J. Mater. Chem. C **11**, 2430–2448 (2023).
[19]H. Kumar and A. K. Pandey, "A simulation-based study of back-illuminated lateral Ge/GeSn/Ge photodetectors on Si platform for mid-infrared image sensing," IEEE Trans. Electron Devices **70**, 1721–1727 (2023).
[20]F. Djeffal and H. Ferhati, "Numerical investigation of a new GeSn MIR phototransistor based on IGZO TFT platform," in *2022 19th International Conference on Electrical Engineering* (Computing Science and Automatic Control, 2022), pp. 1–5.
[21]H. Cong, C. Xue, J. Zheng, F. Yang, K. Yu, Z. Liu, X. Zhang, B. Cheng, and Q. Wang, "Silicon based GeSn p-i-n photodetector for SWIR detection," IEEE Photon. J. **8**, 1–6 (2016).
[22]M. Oehme, K. Kostecki, T. Arguirov, G. Mussler, K. Ye, M. Gollhofer, M. Schmid, M. Kaschel, R. A. Korner, M. Kittler, D. Buca, E. Kasper, and J. Schulze, "Gesn heterojunction LEDs on Si substrates," IEEE Photon. Technol. Lett. **26**, 187–189 (2014).
[23]S. Wirths, R. Geiger, N. von den Driesch, G. Mussler, T. Stoica, S. Mantl, Z. Ikonic, M. Luysberg, S. Chiussi, J. M. Hartmann, H. Sigg, J. Faist, D. Buca, and D. Grützmacher, "Lasing in direct-bandgap GeSn alloy grown on Si," Nat. Photon. **9**, 88–92 (2015).
[24]J. Song, X. Zhao, X. Wu, and R. Xuan, "High rectification efficiency direct bandgap $Ge_{1-x}Sn_x$ Schottky diode for microwave wireless power transfer," Appl. Phys. A **125**, 719 (2019).
[25]S. Prucnal, Y. Berencén, M. Wang, L. Rebohle, R. Böttger, I. A. Fischer, L. Augel, M. Oehme, J. Schulze, M. Voelskow, M. Helm, W. Skorupa, and S. Zhou, "Ex situ $n^+$ doping of GeSn alloys via non-equilibrium processing," Semicond. Sci. Technol. **33**, 065008 (2018).
[26]A. Elbaz, R. Arefin, E. Sakat, B. Wang, E. Herth, G. Patriarche, A. Foti, R. Ossikovski, S. Sauvage, X. Checoury, K. Pantzas, I. Sagnes, J. Chrétien, L. Casiez, M. Bertrand, V. Calvo, N. Pauc, A. Chelnokov, P. Boucaud, F. Boeuf, V. Reboud, J.-M. Hartmann, and M. El Kurdi, "Reduced lasing thresholds in GeSn microdisk cavities with defect management of the optically active region," ACS Photon. **7**, 2713–2722 (2020).
[27]Y. Zhou, W. Dou, W. Du, S. Ojo, H. Tran, S. A. Ghetmiri, J. Liu, G. Sun, R. Soref, J. Margetis, J. Tolle, B. Li, Z. Chen, M. Mortazavi, and S.-Q. Yu, "Optically pumped GeSn lasers operating at 270 K with broad waveguide structures on Si," ACS Photon. **6**, 1434–1441 (2019).
[28]See https://www.nature.com/articles/s41566–020-0601-5 for "Ultra-low-threshold continuous-wave and pulsed lasing in tensile-strained GeSn alloys" (accessed 26 May 2023).
[29]Y. Zhou, Y. Miao, S. Ojo, H. Tran, G. Abernathy, J. M. Grant, S. Amoah, G. Salamo, W. Du, J. Liu, J. Margetis, J. Tolle, Y. Zhang, G. Sun, R. A. Soref, B. Li, and S.-Q. Yu, "Electrically injected GeSn lasers on Si operating up to 100 K," Optica **7**, 924–928 (2020).
[30]See https://www.proquest.com/openview/d68c83679553aa32414dcf300276c3c1/1?pq-origsite=gscholar&cbl=44156 for "Germanium-Tin (GeSn) Technology" (accessed 26 May 2023).
[31]F. Gencarelli, B. Vincent, J. Demeulemeester, A. Vantomme, A. Moussa, A. Franquet, A. Kumar, H. Bender, J. Meersschaut, W. Vandervorst, R. Loo, M. Caymax, K. Temst, and M. Heyns, "Crystalline properties and strain relaxation mechanism of CVD grown GeSn," ECS Trans. **50**, 875 (2013).
[32]H. Mahmodi, M. R. Hashim, and U. Hashim, "Formation of nanocrystalline GeSn thin film on Si substrate by sputtering and rapid thermal annealing," Superlattices Microstruct. **98**, 235–241 (2016).
[33]M. Bauer, J. Taraci, J. Tolle, A. Chizmeshya, S. Zollner, D. Smith, J. Menendez, C. Hu, and J. Kouvetakis, "Ge–Sn semiconductors for band-gap and lattice engineering," Appl. Phys. Lett. **81**, 2992–2994 (2002).
[34]R. Beeler, R. Roucka, A. V. G. Chizmeshya, J. Kouvetakis, and J. Menéndez, "Nonlinear structure-composition relationships in the $Ge_{1-y}Sn_y/Si(100)$ ($y<0.15$)," Phys. Rev. B **84**, 035204 (2011).
[35]A. V. G. Chizmeshya, M. R. Bauer, and J. Kouvetakis, "Experimental and theoretical study of deviations from Vegard's law in the $Sn_xGe_{1-x}$ system," Chem. Mater. **15**, 2511–2519 (2003).
[36]G. Sun, R. A. Soref, and H. H. Cheng, "Design of an electrically pumped SiGeSn/GeSn/SiGeSn double-heterostructure midinfrared laser," J. Appl. Phys. **108**, 033107 (2010).
[37]P. Moontragoon, R. A. Soref, and Z. Ikonic, "The direct and indirect bandgaps of unstrained $Si_xGe_{1-x-y}Sn_y$ and their photonic device applications," J. Appl. Phys. **112**, 073106 (2012).
[38]M. Mysliwiec, M. Sochacki, R. Kisiel, M. Guziewicz, and M. Wzorek, "TiAl-based ohmic contacts on p-type SiC," *IEEE Proceedings of the 2011 34th International Spring Seminar on Electronics Technology (ISSE)* (IEEE, 2011), pp. 68–72.
[39]K. Buchholt, R. Ghandi, M. Domeij, C.-M. Zetterling, J. Lu, P. Eklund, L. Hultman, and A. L. Spetz, "Ohmic contact properties of magnetron sputtered $Ti_3SiC_2$ on n- and p-type 4H-silicon carbide," Appl. Phys. Lett. **98**, 042108 (2011).
[40]K. Toko, N. Oya, N. Saitoh, N. Yoshizawa, and T. Suemasu, "70 °C synthesis of high-Sn content (25%) GeSn on insulator by Sn-induced crystallization of amorphous Ge," Appl. Phys. Lett. **106**, 082109 (2015).
[41]H. Khelidj, A. Portavoce, M. Bertoglio, M. Descoins, L. Patout, K. Hoummada, A. Hallén, A. Charaï, M. C. Benoudia, and D. Mangelinck, "Ge(Sn) growth on Si (001) by magnetron sputtering," Mater. Today Commun. **26**, 101915 (2021).
[42]I. Dascalescu, N. C. Zoita, A. Slav, E. Matei, S. Iftimie, F. Comanescu, A.-M. Lepadatu, C. Palade, S. Lazanu, D. Buca, V. S. Teodorescu, M. L. Ciurea, M. Braic, and T. Stoica, "Epitaxial GeSn obtained by high power impulse magnetron sputtering and the heterojunction with embedded GeSn nanocrystals for shortwave infrared detection," ACS Appl. Mater. Interfaces **12**, 33879–33886 (2020).
[43]J. Zheng, S. Wang, Z. Liu, H. Cong, C. Xue, C. Li, Y. Zuo, B. Cheng, and Q. Wang, "GeSn p-i-n photodetectors with GeSn layer grown by magnetron sputtering epitaxy," Appl. Phys. Lett. **108**, 033503 (2016).
[44]X. Liu, J. Zheng, M. Li, F. Wan, C. Niu, Z. Liu, Y. Zuo, C. Xue, and B. Cheng, "Growth of relaxed GeSn film with high Sn content via Sn component-grade buffer layer structure," J. Phys. D: Appl. Phys. **54**, 435101 (2021).
[45]H. Huang, D. Zhao, C. Qi, J. Huang, Z. Zeng, B. Zhang, and S. Lu, "Effect of growth temperature on crystallization of $Ge_{1-x}Sn_x$ films by magnetron sputtering," Crystals **12**, 1810 (2022).
[46]S. Gupta, R. Chen, B. Magyari-Kope, H. Lin, B. Yang, A. Nainani, Y. Nishi, J. S. Harris, and K. C. Saraswat, "GeSn technology: Extending the Ge electronics roadmap," *IEEE International Electron Devices Meeting* (IEEE, 2011), pp. 16.6.1–16.6.4.
[47]G. Han, S. Su, C. Zhan, Q. Zhou, Y. Yang, L. Wang, P. Guo, W. Wei, C. P. Wong, Z. X. Shen, B. Cheng, and Y. Yeo, "High-mobility germanium-tin (GeSn) P-channel MOSFETs featuring metallic source/drain and sub-370 °C process modules," *IEEE International Electron Devices Meeting* (IEEE, 2011), pp. 16.7.1–16.7.3.
[48]J. K. Efavi, T. Mollenhauer, T. Wahlbrink, H. D. B. Gottlob, M. C. Lemme, and H. Kurz, "Tungsten work function engineering for dual metal gate nano-CMOS," J. Mater. Sci.: Mater. Electron. **16**, 433–436 (2005).
[49]C. Delwail, S. Joblot, F. Mazen, F. Abbate, L. Lachal, F. Milesi, M. Bertoglio, A. M. Papon, M. Gregoire, P. H. Rodriguez, and D. Mangelinck, "Impact of the pre amorphization by Ge implantation on $Ni_{0.9}Pt_{0.1}$ silicide," Microelectron. Eng. **254**, 111705 (2022).
[50]S. Thomas and L. E. Terry, "Composition profiles and Schottky barrier heights of silicides formed in NiPt alloy films," J. Appl. Phys. **47**, 301–307 (1976).
[51]A. Quintero, P. Gergaud, J.-M. Hartmann, V. Reboud, and P. Rodriguez, "Ni-based metallization of GeSn layers: A review and recent advances," Microelectron. Eng. **269**, 111919 (2023).
[52]A. Quintero, P. Gergaud, J.-M. Hartmann, V. Delaye, V. Reboud, E. Cassan, and P. Rodriguez, "Impact and behavior of Sn during the Ni/GeSn solid-state reaction," J. Appl. Crystallogr. **53**, 605–613 (2020).
[53]Y. Chuang, C.-Y. Liu, H.-S. Kao, K.-Y. Tien, G.-L. Luo, and J.-Y. Li, "Schottky barrier height modulation of metal/n-GeSn contacts featuring Low contact resistivity by *in situ* chemical vapor deposition doping and NiGeSn alloy formation," ACS Appl. Electron. Mater. **3**, 1334–1340 (2021).

[54]J. Demeulemeester, A. Schrauwen, O. Nakatsuka, S. Zaima, M. Adachi, Y. Shimura, C. M. Comrie, C. Fleischmann, C. Detavernier, K. Temst, and A. Vantomme, "Sn diffusion during Ni germanide growth on $Ge_{1-x}Sn_x$," Appl. Phys. Lett. **99**, 211905 (2011).
[55]E. Galluccio, N. Petkov, G. Mirabelli, J. Doherty, S.-V. Lin, F.-L. Lu, C. W. Liu, J. D. Holmes, and R. Duffy, "Ni, Pt, and Ti stanogermanide formation on $Ge_{0.92}Sn_{0.08}$," *IEEE Joint International EUROSOI Workshop and International Conference on Ultimate Integration on Silicon (EUROSOI-ULIS)* (IEEE, 2019), pp. 1–4.
[56]A. Quintero, P. Gergaud, N. Chevalier, J. Aubin, J. M. Hartmann, V. Loup, V. Reboud, E. Cassan, and P. Rodriguez, "Impact of Sn content in $Ge_{1-x}Sn_x$ layers on Ni-stanogermanides solid-state reaction and properties," in *2018 IEEE International Interconnect Technology Conference (IITC)* (IEEE, Santa Clara, CA, 2018), pp. 103–105.
[57]A. Quintero, P. Gergaud, J. Aubin, J. M. Hartmann, N. Chevalier, J. P. Barnes, V. Loup, V. Reboud, F. Nemouchi, and P. Rodriguez, "Impact of Pt on the phase formation sequence, morphology, and electrical properties of $Ni(Pt)/Ge_{0.9}Sn_{0.1}$ system during solid-state reaction," J. Appl. Phys. **124**, 085305 (2018).
[58]Y. Liu, H. Wang, J. Yan, and G. Han, "Reduction of formation temperature of Nickel mono-stanogermanide [Ni(GeSn)] by the incorporation of tin," ECS Solid State Lett. **3**, P11 (2013).
[59]F. Nemouchi, "Réactivité de films nanométriques de nickel sur substrats silicium-germanium," These de doctorat (Aix-Marseille, 2005), Vol. **3**, https://theses.fr/2005AIX30052 (accessed 12 April 2024).
[60]S. Gaudet, C. Detavernier, C. Lavoie, and P. Desjardins, "Reaction of thin Ni films with Ge: Phase formation and texture," J. Appl. Phys. **100**, 034306 (2006).
[61]F. Nemouchi, V. Carron, J. L. Lábár, L. Vandroux, Y. Morand, T. Morel, and J. P. Barnes, "Formation of NiGe through germanium oxide on Ge(001) substrate," Microelectron. Eng. **107**, 178–183 (2013).
[62]F. M. d'Heurle and P. Gas, "Kinetics of formation of silicides: A review," J. Mater. Res. **1**, 205–221 (1986).
[63]D. Mangelinck, "Chapter 9—The growth of silicides and germanides," in *Handbook of Solid State Diffusion* (Elsevier, 2017), Vol. 2, pp. 379–446.
[64]W. Kun, A. Nishikata, T. Suzuki, and Y. Mishima, "The Ni–Ge–Sn phase diagram," Z. Metallkd. **81**, 12 (1990) (Germany, F.R), see https://www.osti.gov/etdeweb/biblio/6261273 (accessed 26 May 2023).
[65]D. Mangelinck and K. Hoummada, "Effect of stress on the transformation of $Ni_2Si$ into NiSi," Appl. Phys. Lett. **92**, 254101 (2008).
[66]F. Nemouchi, D. Mangelinck, J. L. Lábár, M. Putero, C. Bergman, and P. Gas, "A comparative study of nickel silicides and nickel germanides: Phase formation and kinetics," Microelectron. Eng. **83**, 2101–2106 (2006).
[67]F. Nemouchi, D. Mangelinck, C. Bergman, P. Gas, and U. Smith, "Differential scanning calorimetry analysis of the linear parabolic growth of nanometric Ni silicide thin films on a Si substrate," Appl. Phys. Lett. **86**, 041903 (2005).
[68]C. Perrin, D. Mangelinck, F. Nemouchi, J. Labar, C. Lavoie, C. Bergman, and P. Gas, "Nickel silicides and germanides: Phases formation, kinetics and thermal expansion," Mater. Sci. Eng. B **154–155**, 163–167 (2008).
[69]P. Gergaud, O. Thomas, and B. Chenevier, "Stresses arising from a solid state reaction between palladium films and Si(001) investigated by *in situ* combined x-ray diffraction and curvature measurements," J. Appl. Phys. **94**, 1584–1591 (2003).
[70]C. Rivero, P. Gergaud, M. Gailhanou, O. Thomas, B. Froment, H. Jaouen, and V. Carron, "Combined synchrotron x-ray diffraction and wafer curvature measurements during Ni–Si reactive film formation," Appl. Phys. Lett. **87**, 041904 (2005).
[71]C. Rivero, P. Gergaud, M. Gailhanou, P. Boivin, P. Fornara, S. Niel, and O. Thomas, "Stress development and relaxation during reaction of a cobalt film with a silicon substrate," Defect Diffus. Forum **237–240**, 518–523 (2005).
[72]S.-L. Zhang and F. M. d'Heurle, "Stresses from solid state reactions: A simple model, silicides," Thin Solid Films **213**, 34–39 (1992).
[73]A. Steegen and K. Maex, "Silicide-induced stress in Si: Origin and consequences for MOS technologies," Mater. Sci. Eng. R **38**, 1–53 (2002).
[74]P. Gergaud, M. Megdiche, O. Thomas, and B. Chenevier, "Influence of Si substrate orientation on stress development in Pd silicide films grown by solid-state reaction," Appl. Phys. Lett. **83**, 1334–1336 (2003).
[75]See https://www.scientific.net/DDF.237-240.801 for "Stress development during the reactive formation of silicide films" (accessed 12 April 2024).
[76]See https://www.scientific.net/DDF.129-130.137 for "Stresses during silicide formation: A review" (accessed 12 April 2024).
[77]D. Mangelinck, J. Y. Dai, J. S. Pan, and S. K. Lahiri, "Enhancement of thermal stability of NiSi films on (100)Si and (111)Si by Pt addition," Appl. Phys. Lett. **75**, 1736–1738 (1999).
[78]F. M. d'Heurle, P. Gas, and J. Philibert, "Diffusion–reaction: The ordered $Cu_3Au$ rule and its corollaries," Solid State Phenom. **41**, 93–102 (1995).
[79]C. Lavoie, C. Detavernier, C. Cabral, Jr., F. M. d'Heurle, A. J. Kellock, J. Jordan-Sweet, and J. M. E. Harper, "Effects of additive elements on the phase formation and morphological stability of nickel monosilicide films," Microelectron. Eng. **83**, 2042–2054 (2006).
[80]K. Hoummada, C. Perrin-Pellegrino, and D. Mangelinck, "Effect of Pt addition on Ni silicide formation at low temperature: Growth, redistribution, and solubility," J. Appl. Phys. **106**, 063511 (2009).
[81]M. Liu and R. Y. Wang, "Size-dependent melting behavior of colloidal In, Sn and Bi nanocrystals," Sci. Rep. **5**, 16353 (2015).
[82]M. Friesel, U. Södervall, and W. Gust, "Diffusion of tin in germanium studied by secondary ion mass spectrometry," J. Appl. Phys. **78**, 5351–5355 (1995).
[83]E. Hüger, U. Tietze, D. Lott, H. Bracht, D. Bougeard, E. E. Haller, and H. Schmidt, "Self-diffusion in germanium isotope multilayers at low temperatures," Appl. Phys. Lett. **93**, 162104 (2008).
[84]A. Quintero, P. Gergaud, N. Chevalier, J. Aubin, J.M. Hartmann, V. Loup, V. Reboud, E. Cassan, and P. Rodriguez, "Impact of Sn content in $Ge_{1-x}Sn_x$ layers on Ni-stanogermanides solid-state reaction and properties," in *2018 IEEE International Interconnect Technology Conference (IITC)* (IEEE, 2018), pp. 103–105.
[85]M. A. Rahman, T. Osipowicz, D. Z. Chi, and W. D. Wang, "Observation of a new kinetics to form $Ni_3Si_2$ and $Ni_{31}Si_{12}$ silicides at low temperature (200 °C)," J. Electrochem. Soc. **152**, G900 (2005).